NASA
Technical
Paper
3197

June 1992

Calculation of Unsteady Transonic Flows With Mild Separation by Viscous-Inviscid Interaction

James T. Howlett

NASA Technical Paper 3197

1992

Calculation of Unsteady Transonic Flows With Mild Separation by Viscous-Inviscid Interaction

James T. Howlett
Langley Research Center
Hampton, Virginia

NASA
National Aeronautics and Space Administration
Office of Management
Scientific and Technical Information Program

Summary

This paper presents a method for calculating viscous effects on two- and three-dimensional unsteady transonic flow fields. An integral boundary-layer method for turbulent viscous flow is coupled with the transonic small-disturbance potential equation in a quasi-steady manner. The boundary-layer calculation uses Green's lag-entrainment equations for attached flow and an inverse boundary-layer method for flows with mild separation. Three-dimensional viscous effects are approximated by a stripwise application of the two-dimensional boundary-layer equations. The method is demonstrated for several test cases, including two-dimensional airfoils and a three-dimensional wing configuration. The applications for two-dimensional airfoils include an example that illustrates the method for calculating aileron buzz and thus demonstrates the present method for analyzing a key aeroelastic problem. Comparisons with inviscid calculations, other viscous calculation methods, and experimental data are presented. The results demonstrate that the present technique can economically and accurately calculate unsteady transonic flow fields having viscous-inviscid interactions with mild flow separation.

Introduction

Computational methods for accurately calculating unsteady transonic flow for aeroelastic applications are rapidly maturing (ref. 1). For example, Malone, Sankar, and Sotomayer (ref. 2) calculated unsteady air loads on the F-5 fighter wing with a full-potential computer code, Steger and Bailey (ref. 3) calculated aileron buzz with a Navier-Stokes code, and Anderson and Batina (ref. 4) calculated unsteady pressure distributions for both two- and three-dimensional configurations with an Euler code and a transonic small-disturbance potential code called CAP-TSD (Computational Aeroelasticity Program-Transonic Small Disturbance) (ref. 5). Other applications of Euler codes and Navier-Stokes codes illustrate the complex flow phenomena that can be computed by these methods. However, full-potential, Euler, and Navier-Stokes codes usually require large amounts of computer time and, as a result, are currently too expensive for routine applications. Thus, substantial efforts have been devoted to the development of transonic small-disturbance codes (ref. 6).

For flows involving weak or moderately strong embedded shock waves, inviscid calculations that use the TSD equations have produced accurate solutions in many cases: thin airfoils (ref. 7), thin wings (ref. 8), wing-canard combinations (ref. 9), and realistic aircraft configurations (ref. 6). As shock waves increase in strength and move aft on the airfoil, viscous effects become significant and must be accounted for in the computations to obtain accurate solutions (ref. 10). For flows that remain attached, integral boundary-layer methods may be coupled with the inviscid analysis by viscous-inviscid iteration. These interactive boundary-layer techniques have produced viscous solutions that agree well with experimental results (refs. 11 to 14).

For separated flows, integral techniques are also available. In particular, LeBalleur (ref. 15) developed a fully unsteady viscous-inviscid integral technique. Good results were achieved when LeBalleur and Girodroux-Lavigne (ref. 16) applied the technique to several airfoils that had strong viscous-inviscid interactions and extensive regions of flow separation. (See ref. 16.) The technique, however, can require large computer resources; some cases in reference 16 required up to 15 viscous-inviscid iterations at each time step to obtain converged solutions. Melnik and Brook (ref. 17) specialized LeBalleur's technique, with some modifications, to steady calculations for inclusion in the GRUMFOIL computer code. Calculations made with this code agree reasonably with experimental data up to and slightly beyond maximum lift.

This paper presents an efficient method for calculating viscous effects on two- and three-dimensional configurations for unsteady transonic turbulent flows. The inverse boundary-layer method in reference 17 is incorporated into the CAP-TSD computer code (refs. 5, 18, and 19) in a quasi-steady manner. Carter's method (ref. 20) is used to couple the inverse calculations with the inviscid algorithm. Green's lag-entrainment equations are included to calculate attached flows. The resulting computer code is applied to several test cases, including both two-dimensional airfoils and a three-dimensional wing configuration. The results demonstrate that the present technique can economically and accurately calculate unsteady transonic flow fields involving viscous-inviscid interactions with mild flow separation.

Symbols and Abbreviations

CAP-TSD	Computational Aeroelasticity Program-Transonic Small Disturbance
C_E	entrainment coefficient
C_f	skin-friction coefficient
C_p	pressure coefficient

$\widetilde{C}_p$	normalized unsteady pressure coefficient; first harmonic of C_p divided by oscillation amplitude
C_τ	shear stress coefficient
c	airfoil chord, m
c_l	lift coefficient
c_m	pitching-moment coefficient about quarter-chord
EXP	experimental
f	oscillation frequency, Hz
$f_0, \ldots, f_3$	functions in transonic small-disturbance equation defined by equation (2)
H, H_1, $\overline{H}$	boundary-layer shape factors
k	reduced frequency, $\omega c/2U$
M	free-stream Mach number
$\overline{m}$	$= \rho_e U_e \delta^*$
$N_{\mathrm{Pr},t}$	turbulent Prandtl number
N_{Re}	Reynolds number, Uc/ν
N_{Su}	Sutherland number
q	dynamic pressure, psf
R_1, R_2, R_3	constants in equations (9) to (11)
r	$= N_{\mathrm{Pr},t}^{1/3}$
S	airfoil surface function
t	nondimensional time, $\frac{U}{c}\bar{t}$
Δt	nondimensional time step
$\bar{t}$	time, sec
U	free-stream velocity, m/sec
U_m	magnitude of reverse flow in boundary layer
U_v	streamwise velocity of viscous flow in boundary layer
x, y, z	Cartesian coordinates in streamwise, spanwise, and vertical directions
α	angle of attack, deg
α_0	mean angle of attack, deg
α_1	dynamic pitch angle, deg
$\overline{\alpha}$	$= \delta^*/\delta$
β	flap angle, deg
γ	ratio of specific heats
$\Delta(\ldots)$	indicates jump in ...
δ	boundary-layer thickness, m
δ^*	boundary-layer displacement thickness, m
η	$= z/\delta$
$\overline{\eta}$	$= (\eta - \eta^*)/(1 - \eta^*)$
η_s	fraction of semispan
η^*	height of reversed flow region
θ	boundary-layer momentum thickness, m
ν	kinematic viscosity, $\mathrm{m}^2/\mathrm{sec}$
ρ	density
ϕ	inviscid-disturbance velocity potential
ω	relaxation factor

Subscripts:

B	aileron buzz
e	boundary-layer edge
i	inviscid quantity
le	leading edge
te	trailing edge
v	viscous quantity

All angles are positive for trailing edge down. Moments are positive for leading edge up. Hinge moments are taken about the hinge axis.

Governing Equations

The inviscid flow code used in this analysis is the transonic small-disturbance potential computer code CAP-TSD developed at NASA Langley Research Center by Batina et al. (refs. 5, 18, and 19). The CAP-TSD code uses an approximate factorization algorithm (ref. 18) for time-accurate solution of the unsteady TSD equation. The code has been applied extensively to airfoils (refs. 4 and 18), wings (ref. 21), wing-body configurations (ref. 5), and complete aircraft configurations (ref. 6). These references include comparisons with experiments as well as with other computer codes for computational fluid dynamics.

The viscous analysis presented in this paper interactively couples the CAP-TSD inviscid flow code with an integral boundary-layer technique to model turbulent viscous flow effects. The direct boundary-layer method for attached flow is based upon Green's lag-entrainment equations and is a modified application of the method described in reference 14. The equations are repeated herein for completeness. The inverse boundary-layer equations are based upon the work of Melnik and Brook (ref. 17) and are included in the CAP-TSD computer code in a stripwise manner.

Inviscid Equations

The CAP-TSD computer code solves the modified transonic small-disturbance equation in conservative form

$$\frac{\partial f_0}{\partial t} + \frac{\partial f_1}{\partial x} + \frac{\partial f_2}{\partial y} + \frac{\partial f_3}{\partial z} = 0 \tag{1}$$

where ϕ is the inviscid-disturbance velocity potential:

$$f_0 = -A\phi_t - B\phi_x \tag{2a}$$

$$f_1 = E_1\phi_x + F_1\phi_x^2 + G_1\phi_y \tag{2b}$$

$$f_2 = \phi_y + H_1\phi_x\phi_y \tag{2c}$$

$$f_3 = \phi_z \tag{2d}$$

The coefficients A, B, and E_1 are defined as

$$A = M^2 \qquad B = 2M^2 \qquad E_1 = 1 - M^2$$

Choices for the coefficients F_1, G_1, and H_1 depend upon the assumption used to derive the TSD equations. In this paper, the two-dimensional calculations are made with the following "NLR" coefficients (ref. 22):

$$F_1 = -\frac{1}{2}\left[3 - (2-\gamma)M^2\right]M^2$$

$$G_1 = -\frac{1}{2}M^2$$

$$H_1 = -M^2$$

For the three-dimensional calculations, the following "NASA Ames" coefficients (ref. 22) are used:

$$F_1 = -\frac{1}{2}(\gamma+1)M^2$$

$$G_1 = \frac{1}{2}(\gamma-3)M^2$$

$$H_1 = -(\gamma-1)M^2$$

Also, the CAP-TSD code incorporates modifications to the coefficients in equations (2); these modifications were developed by Batina (ref. 19) to approximate the effects of shock generated entropy or vorticity.

The boundary conditions on the wing and wake are

$$\phi_z^{\pm} = S_x^{\pm} + S_t^{\pm} \qquad \left(x_{le} \le x \le x_{te};\ z = 0^{\pm}\right) \tag{3}$$

$$\Delta\phi_z = 0 \qquad \left(x > x_{te};\ z = 0^{\pm}\right) \tag{4}$$

$$\Delta\left(\phi_x + \phi_t\right) = 0 \qquad \left(x > x_{te};\ z = 0^{\pm}\right) \tag{5}$$

where the superscript $\pm$ refers to the wing upper or lower surface, the function $S(x,t)$ denotes the wing surface, and $\Delta(\ldots)$ indicates a jump in the bracketed quantity across the wake. In the far field, nonreflecting boundary conditions similar to the ones developed by Whitlow (ref. 23) are implemented in the CAP-TSD code. References 6 and 23 contain details of the derivation of those boundary conditions.

Viscous Equations for Attached Flow

The effect of a turbulent viscous boundary layer for attached flow is modeled in a quasi-steady manner by Green's lag-entrainment equations as implemented in reference 14. References 14 and 24 present additional details. The boundary-layer equations for attached flow are

$$\frac{d\theta}{dx} = \frac{1}{2}C_f - \left(H + 2 - M_e^2\right)\theta\phi_{xx} \tag{6}$$

$$\theta\frac{d\overline{H}}{dx} = \left(C_E - \frac{1}{2}H_1C_f\right)\frac{d\overline{H}}{dH_1} + H_1(H+1)\frac{d\overline{H}}{dH_1}\theta\phi_{xx} \tag{7}$$

$$\theta\frac{dC_E}{dx} = F\left\{\frac{2.8}{H+H_1}\left[(C_\tau)_{\mathrm{EQO}} - \lambda C_\tau^{1/2}\right] + \left(\frac{\theta}{U_e}\frac{dU_e}{dx}\right)_{\mathrm{EQ}}\right\}$$

$$- F\left(1 + 0.075M_e^2\frac{1 + \frac{\gamma-1}{2}rM_e^2}{1 + 0.1M_e^2}\right)\theta\phi_{xx} \tag{8}$$

Equation (8) for the entrainment coefficient is taken from reference 12 and differs slightly from the equation given in reference 24. The surface velocity gradient ϕ_{xx} is smoothed for numerical stability during the computations as discussed in reference 14. The subscript e in these equations refers to quantities at the boundary-layer edge, the subscript EQ denotes the equilibrium conditions, and the subscript

EQO denotes the equilibrium conditions in the absence of secondary influences on the turbulence structure (ref. 24). The various parameters in these equations $\left(\text{i.e., } C_f,\ F,\ H,\ H_1,\ M_e,\ C_\tau,\ r,\ \left(\frac{\theta}{U_e}\frac{dU_e}{dx}\right)_{\text{EQ}},\ \text{and } (C_\tau)_{\text{EQO}}\right)$ are defined in the appendix.

Viscous Equations for Separated Flow

In flow fields that contain regions of separation, the boundary-layer equations are written in inverse form. Thus, these equations can be solved when given a specified streamwise variation of boundary-layer displacement thickness as represented by a perturbation mass flow parameter $\overline{m} = \rho_e U_e \delta^*$. The solution to the inverse equations (i.e., the viscous velocity at the edge of the boundary layer) is then used in a relaxation formula to update the displacement thickness and calculate a new value of $\overline{m}$. This iterative process is repeated at each time step until convergence is achieved. This particular inverse form of the boundary-layer equations was developed by Vatsa and Carter at the United Technologies Research Center, and it is completely compatible with Green's original lag-entrainment equations in regions of attached flow. The inverse equations are

$$\frac{1}{U_e}\frac{dU_e}{dx} = \frac{\frac{-1}{\overline{m}}\frac{d\overline{m}}{dx} + \frac{1}{H\theta}R_1\frac{d\overline{H}}{dH_1}\left(C_E - \frac{1}{2}C_f H_1\right) + \frac{1}{2}\frac{C_f}{\theta}}{(H+1)\left\{1 - \frac{R_1}{H}\left[\frac{(\gamma-1)rM_e^2R_2}{R_1^2} + H_1\frac{d\overline{H}}{dH_1}\right]\right\}} \tag{9}$$

$$\frac{d\overline{H}}{dx} = \frac{\frac{d\overline{H}}{dH_1}\left\{\frac{1}{\theta}\left(C_E - \frac{1}{2}C_f H_1\right)\left[1 - \frac{R_1(\gamma-1)rM_e^2R_2}{HR_1^2}\right] - H_1\left(\frac{1}{\overline{m}}\frac{d\overline{m}}{dx} - \frac{1}{2}\frac{C_f}{\theta}\right)\right\}}{1 - \frac{R_1}{H}\left[\frac{(\gamma-1)rM_e^2R_2}{R_1^2} + H_1\frac{d\overline{H}}{dH_1}\right]} \tag{10}$$

$$\theta\frac{dC_E}{dx} = F\left\{\frac{R_3}{H+H_1}\left[(C_\tau)_{\text{EQO}}^{1/2} - \lambda\,(C_\tau)^{1/2}\right] + \left(\frac{\theta}{U_e}\frac{dU_e}{dx}\right)_{\text{EQ}} - \theta\phi_{xx}\left[1 + 0.075M_e^2\frac{R_1}{1+0.1M_e^2}\right]\right\} \tag{11}$$

where $R_1 = 1 + \frac{\gamma-1}{2}rM_e^2$ and $R_2 = 1 + \frac{\gamma-1}{2}M_e^2$. Defined in the following section, R_3 is a factor that provides transition between the equations for attached flow and separated flow.

The subscript e in these equations refers to quantities at the boundary-layer edge, the subscript EQ denotes equilibrium conditions, and the subscript EQO denotes equilibrium conditions in the absence of secondary influences on the turbulent structure. (See ref. 24.) The parameters that appear in equations (9) to (11) are defined in the following section.

Closure Conditions for Inverse Boundary Layer

The inverse boundary-layer equations contain additional unknowns that must be specified by further assumptions (closure conditions) before the equations can be solved. For separated flow, these closure conditions are based upon the work of Melnik and Brook (ref. 17), which closely follows the analysis of LeBalleur in reference 15, where additional details may be found.

The separated flow is represented by a detached free-shear layer that is separated from the airfoil by a region of constant velocity reverse flow. The velocity profile (fig. 1) used to model the flow in the separated region is given by

$$\frac{U_v}{U_e} = 1 - C_2 F_p(\eta)$$

where

$$C_2 = \frac{\overline{\alpha}}{a_1(1 + a_2\eta^*)} \qquad \left(a_1 = \frac{1}{2};\ a_2 = 1\right)$$

$$\overline{\alpha} = \frac{\delta^*}{\delta}$$

$$F_p(\eta) = 1 \qquad (0 \le \eta \le \eta^*)$$

$$F_p(\eta) = F_c(\overline{\eta}) \qquad (\eta^* < \eta \le 1)$$

$$\eta = \frac{z}{\delta}$$

$$\overline{\eta} = \frac{\eta - \eta^*}{1 - \eta^*}$$

The parameter $\overline{\alpha}$ is determined by an iterative process described in a subsequent section of this paper. The function $F_c(\overline{\eta})$ is Cole's wake function:

$$F_c(\overline{\eta}) = \frac{1}{2}(1 + \cos \pi \overline{\eta})$$

The magnitude of the reversed flow is $U_m/U_e = 1 - C_2$. Following Melnik and Brook, η^* is given by

$$\eta^*(\overline{\alpha}) = \begin{cases} b\overline{\alpha} + (1-b) & (\alpha_m \le \overline{\alpha} \le 1) \\ a(\overline{\alpha} - \alpha_s)^2 & (\alpha_s < \overline{\alpha} < \alpha_m) \\ 0 & (\overline{\alpha} \le \alpha_s) \end{cases}$$

where

$$b = 2.1$$

$$a = \frac{b}{4(1 - a_1 - b^{-1})}$$

$$\alpha_s = a_1$$

$$\alpha_m = 2\left(1 - \frac{1}{2}a_1\right) - 2b^{-1}$$

The above assumptions, along with a mixing length formula for the Reynolds stresses, provide all information required for the following closure conditions (ref. 17):

$$\overline{H}(\overline{\alpha}) = \{1 - [1 + B(\eta^*)]\overline{\alpha}\}^{-1} \qquad (12)$$

where

$$B(\eta^*) = \frac{G_2(\eta^*)}{G_1^2(\eta^*)} - 1$$

$$G_1(\eta^*) = a_1(1 + a_2\eta^*)$$

$$G_2(\eta^*) = b_1(1 + b_2\eta^*)$$

$$b_1 = \frac{3}{8}$$

$$b_2 = \frac{5}{3}$$

$$H_1(\overline{\alpha}) = \overline{H}(\overline{\alpha})\left(\frac{1}{\overline{\alpha}} - 1\right) \qquad (13)$$

$$(C_E)_{\mathrm{EQO}} = \pi^2 0.0064 C_2$$

The derivative $\frac{d\overline{H}}{dH_1} = \frac{1}{\frac{dH_1}{d\overline{H}}}$ is calculated as follows:

$$\frac{dH_1}{d\overline{H}} = \frac{\partial H_1}{\partial \overline{H}} + \frac{\partial H_1}{\partial \overline{\alpha}}\frac{\partial \overline{\alpha}}{\partial \overline{H}} = \frac{\partial H_1}{\partial \overline{H}} + \frac{\partial H_1/\partial \overline{\alpha}}{\partial \overline{H}/\partial \overline{\alpha}}$$

The following equation for the skin friction C_f is the one used by Thomas in reference 25:

$$C_f = \begin{cases} \frac{0.3e^{-1.33H}}{\left(\log_{10} N_{\mathrm{Re},\theta}\right)^{1.74+0.31H}} \\ \quad + (0.00011)\left[\tanh\left(4 - \frac{H}{0.875}\right) - 1\right] & \left(\overline{H} < 2.4\right) \\ 0 & \left(\overline{H} \ge 2.4\right) \end{cases}$$

$$\lambda = \begin{cases} \frac{1}{1-\eta^*} & \text{(On airfoil)} \\ \frac{1}{2}\frac{1}{1-\eta^*} & \text{(On wake)} \end{cases}$$

where $\eta^* = 0$ for attached flow.

The following expression for the factor R_3 of equation (11) is used to provide a transition between the value used in reference 24 and the expression given in reference 17:

$$R_3 = \begin{cases} 2.8 & \left(\overline{H} \le 2\right) \\ \frac{0.15}{\left(1 - \frac{C_2}{2}\right)(0.8)(1-\eta^*)} & \left(\overline{H} > 2\right) \end{cases}$$

The expressions for the remaining parameters are identical to those given in the appendix. The equations for F, C_τ, and $(C_\tau)_{\mathrm{EQO}}$ are slightly different from the corresponding equations in reference 17. The changes are based upon personal communications with R. E. Melnik, the first author of reference 17. As a result of these communications, the new expressions are used in both the direct method and the inverse method.

Viscous Boundary Conditions and Wake

The coupling between the viscous boundary layer and the inviscid analysis is through the boundary conditions on the airfoil and wake. The boundary conditions given by equations (3) and (4) are modified as follows:

$$\phi_z^{\pm} = S_x^{\pm} + S_l^{\pm} + \delta_x^{*\pm} \qquad \left(x_{le} \le x \le x_{te};\ z = 0^{\pm}\right) \qquad (14)$$

$$\Delta\phi_z = \Delta(\delta_x^*) \qquad \left(x > x_{te};\ z = 0^{\pm}\right) \qquad (15)$$

where δ^* is the boundary-layer displacement thickness, the superscript $\pm$ refers to the upper or lower surface of the airfoil, and the $\Delta(\ldots)$ denotes a jump

in the bracketed quantity across the wake. Equation (14) does not include δ_t^* because of the quasi-steady assumption in the boundary-layer equations.

Numerical Implementation

From the leading edge of the airfoil or wing, the boundary layer is approximated by the turbulent boundary layer on a flat plate. At a user-specified point, typically 10 percent chord, numerical integration of the direct boundary-layer equations (6) to (8) is implemented with a fourth-order Runge-Kutta method. Downstream integration of the direct boundary-layer equations continues until the flow nears separation, at which point the method switches to the inverse boundary-layer equations (9) to (11). In the present application, the switch to the inverse equations occurs at $\overline{H} = 1.5$. The inverse calculation continues several chord lengths into the wake, even if the value of $\overline{H}$ drops below the switch value. The inverse equations can also be initiated at a user-specified point along the chord once integration of the direct equations has begun.

At each time step, the inverse boundary-layer algorithm solves equation (12) by Newton iteration for $\overline{\alpha}$, given $\overline{H}$. Then H_1 is determined from equation (13) and the other parameters are computed. The CAP-TSD code also includes a subiteration capability as part of the basic solution algorithm. With the boundary-layer calculations included, this subiteration results in successive viscous-inviscid iterations until the specified level of convergence has been achieved.

Coupling between the inviscid outer flow solution and the direct boundary-layer calculation is straightforward. Once the boundary-layer parameters are computed, the displacement thickness δ^* required by the boundary conditions in equations (14) and (15) is given by

$$\delta^* = \theta H$$

For the inverse boundary-layer calculation, the displacement thickness δ^* is computed by Carter's method (ref. 20):

$$\delta^*_{\text{new}} = \delta^*_{\text{old}} + \omega \delta^*_{\text{old}} \left(\frac{U_{e_v}}{U_{e_i}} - 1 \right)$$

where

ω relaxation factor (typically 0.1 to 0.001)

U_{e_i} inviscid velocity at boundary-layer edge

U_{e_v} viscous velocity at boundary-layer edge

For the time-accurate calculations in this paper, values of ω larger than 0.1 led to instabilities, although values larger than 1.0 are reported in reference 20, where only steady flow solutions are computed.

Results and Discussion

The present method has been applied to several test cases to evaluate its accuracy and range of applicability. Some of these test cases, such as the NACA 64A010A and the NACA 0012 airfoil, have been calculated with previous codes (ref. 14) and are presented to confirm the accuracy of the present method as well as to demonstrate the improvements that have been obtained. The results for the buzz calculations for the airfoil on the P-80 aircraft represent new applications of transonic small-disturbance theory with viscous-inviscid interaction. Figure 2 contains profiles of the configurations studied. The NACA 64A010A airfoil has the coordinates of the section tested at the NASA Ames Research Center (ref. 26); this section had a small amount of camber and was slightly thicker than the symmetrical design section.

Unless otherwise stated, the results for the two-dimensional calculations were obtained on a 142×84 grid in x-z space. This grid extends ± 20 chords in x and ± 25 chords in z; it has 76 points on the airfoil. Also, the vorticity modeling option in the CAP-TSD computer code was turned on for all calculations except those for the airfoil on the P-80.

NACA 64A010A Airfoil

Ten AGARD computational test cases for the NACA 64A010A airfoil were calculated with a previous version of the viscous-inviscid method (XTRAN2L) and compared with experimental results in reference 14. In the present paper, the five cases that show the effect of frequency on unsteady lift and pitching-moment coefficients (i.e., cases 3 to 7 listed in table I) are recalculated with the new computer code, and the results are compared with the previous calculations as well as with the experimental results (ref. 26). The Mach number for these five cases was 0.796, the mean angle of attack was 0°, and the unsteady amplitude of harmonic oscillation was about 1°. The number of time steps per cycle used for the calculation was 720, the relaxation factor ω for the inverse calculations was 0.01, and the maximum number of subiterations was 20 with a convergence criterion of 0.0001.

Figure 3 presents comparisons of the real and imaginary parts of the lift coefficient, and figure 4

presents similar comparisons of the pitching-moment coefficient (about the leading edge). In general, the CAP-TSD viscous results for the lift coefficient agree well with the experimental data. The real part of the lift coefficient is slightly overpredicted, and a small discrepancy exists in the imaginary part for intermediate frequencies. The imaginary part of the lift coefficient for the two lower frequencies (cases 3 and 4) shows considerable improvement over the previous calculations. An examination of the response time histories for the present results compared with those of previous calculations for cases 3 and 4 suggests that accurate calculation of the lift coefficient for these cases depends upon accurate calculation of a small separation bubble that develops at the base of the shock during the unsteady motion.

As figure 4 shows, calculated results for the real part of the pitching-moment coefficient have the same trends with increasing frequency as the experimental data, although the magnitudes are somewhat different. The overprediction of the real part of the pitching-moment coefficient is consistent with the overprediction of the real part of the lift coefficient mentioned previously. The calculated imaginary part of the pitching-moment coefficient agrees fairly well with the experimental results with the largest differences at the higher frequencies.

NACA 0012 Airfoil

The four AGARD cases for the NACA 0012 airfoil (table II) involve larger mean angles of attack (up to 4.86°) and larger amplitude pitch oscillations (up to 4.59°) than are normally considered appropriate for calculations with transonic small-disturbance theory. Calculated results for these cases are presented to investigate the range of applicability of the present theory. The grid for the NACA 0012 calculations is 137×84 in x-z space, has 55 points on the airfoil, and extends ± 20 chords in all directions. The relaxation factor ω for the inverse calculations was 0.001, and the maximum number of subiterations was 20 with a convergence criterion of 0.0001. The number of time steps per cycle used for the calculation was 2048, and results were output every 32 time steps. For most time steps the convergence criterion was satisfied with 2 to 5 iterations, although all 20 iterations were usually required near the maximum angle of attack.

Although viscous effects upstream of the shock are important physically, the interactive boundary layer tended to overpredict viscous effects when the boundary layer was initiated upstream of the shock. This overprediction can be the result of a laminar boundary layer upstream of the shock with transition to turbulence at the shock. Because the present method assumes a turbulent boundary layer, the boundary layer was initiated downstream of the shock position. Because a change in shock position occurs during a cycle of motion, the boundary layer was initiated just downstream of the most rearward position of the shock during a cycle of oscillation. The exact location was determined by trial and error, and the inverse boundary layer was used from that point downstream. As subsequently shown, this approach slightly underpredicts the viscous effects but yields overall results that agree well with the experimental data.

Figures 5 to 9 compare the viscous calculations, inviscid calculations, and experimental data in reference 27. Comparisons were made for instantaneous pressure distributions as well as for lift and moment coefficients versus angle of attack. Because of the difficulty in determining an appropriate time axis for the instantaneous pressure distribution comparisons during a harmonic oscillation, the experimental results were Fourier analyzed to determine phase angles for each of the experimental points. The available calculated results with the nearest phase angles were used for the comparisons.

Figure 5 presents plots of the lift and pitching-moment coefficients versus α for the oscillatory cases 1, 2, 3, and 5. For cases 1 and 2, the viscous lift coefficient is slightly higher than the experimental data near the maximum angle of attack but agrees well with the experimental results elsewhere. For case 3, the viscous lift coefficient is slightly higher than the experimental results over the entire range of angles. For case 5, both the inviscid and viscous calculations give similar results. The lift coefficient is slightly lower than the experiment. Although the Mach number for case 5 is higher than those for the other cases, the mean angle of attack is lower and the shock is weaker. (See fig. 9.) Thus, the effect of the boundary layer is almost negligible. For cases 1 to 3, the viscous lift and moment coefficients agree much better with the experimental results than do the inviscid calculations.

The instantaneous pressure coefficients for cases 1, 2, 3, and 5 are compared in figures 6 to 9. In general, both the inviscid and viscous calculations compare well with the experimental data. The most noticeable difference between the calculated values and the experimental results is the overprediction of the leading-edge suction pressure by both inviscid and viscous calculations. This overprediction of leading-edge pressure was not present in previous calculations with the inviscid code by Batina (ref. 19).

The source of the discrepancy is not known, although it may result from the different grids used in the calculations. During the quarter cycle after maximum α (figs. 6(c), 7(c), and 8(d)), the shock position for the viscous calculation is noticeably better than that for the inviscid calculation as a result of separation effects. Otherwise, the viscous and inviscid results are comparable. For case 5, the viscous and inviscid results are essentially the same.

The results presented herein for the NACA 0012 airfoil demonstrate that transonic small-disturbance theory with an interactive inverse boundary layer can predict with reasonable accuracy the air loads due to moderately large-amplitude pitch oscillations.

P-80 Aileron Buzz

Flight test measurements on the P-80 fighter that were conducted during the mid 1940's demonstrated that a limit cycle oscillation of the aileron control surfaces occurred during transonic flight conditions (ref. 28). This limit cycle oscillation of control surfaces is commonly referred to as aileron buzz. Wind tunnel measurements of a partial span P-80 wing were performed in the NASA Ames 16-Foot High-Speed Wind Tunnel and demonstrated that the basic physical mechanism driving the oscillation is a lag in hinge moment that follows control surface displacement (ref. 29). A two-dimensional calculation that used the P-80 airfoil section shown in figure 2, an NACA 65_1-213 ($a = 0.5$) airfoil, was performed in reference 3 with a Navier-Stokes method for the aerodynamic loads. Although the calculations by Steger and Bailey were exploratory, they demonstrated that aileron buzz can be studied with Navier-Stokes calculations. In the present paper, numerical results demonstrate that aileron buzz can also be investigated through use of transonic small-disturbance theory with an interactive inverse boundary layer. The aileron is modeled as a single control surface mode shape pitching about the three-quarter-chord location. The physical quantities that define the model are taken from reference 28: Moment of inertia = 0.4083 ft-lb/sec^2, Mean chord = 4.83 ft, and Aileron span = 7.5 ft.

The P-80 calculations that were performed included the effects of shock generated entropy, and the inverse boundary-layer calculation was initiated at 12 percent chord. A weak spring was inserted at the aileron hinge because the computer code does not allow zero spring stiffness. The Reynolds number used in the calculations was 20.0 million. No subiterations were used during the calculations and the relaxation factor ω was 0.1. Results were calculated for three values of α_0 ($-1°$, $0°$, $+1°$), and the time step was varied from 214 to 825 steps per cycle as subsequently discussed. To determine aileron buzz, a steady solution was first calculated at a Mach number close to the anticipated buzz condition. This steady solution was then used as a starting solution for an aeroelastic calculation with the dynamic pressure q fixed. The Mach number was varied until a buzz oscillation was obtained with the aileron released from its undeflected position. This procedure does not necessarily determine the minimum Mach number for the onset of aileron buzz. According to reference 3, buzz can be induced by releasing the aileron from a deflected position at conditions where it did not buzz when released from the undeflected position.

The buzz calculations were found to be highly nonlinear. Small changes in the parameters of the problem can significantly affect the numerical results. The nonlinear variation of static hinge moment with Mach number is undoubtedly responsible for much of the nonlinearity. As noted in reference 29, in the transonic speed range the "hinge moments are a sensitive function of Mach number." The present analysis confirms this observation. Figure 10 shows the calculated aileron hinge moment versus Mach number for three airfoil angles of attack. These results are for steady flow conditions with the aileron held fixed at its undeflected position. As figure 10 shows, for Mach numbers higher than 0.78, the aileron hinge moment is highly nonlinear. This strong nonlinearity results in unsteady flow solutions that are sensitive to some of the parameters used to obtain the numerical results. This effect is discussed further in the following paragraphs.

Figure 11 shows the steady pressure distributions of the upper and lower surfaces for $M = 0.82$ and $\alpha = 0°$. The shock on the upper surface is at 78 percent chord, just downstream of the aileron hinge line. The lower surface shock is at 67 percent chord. The difference between the upper and lower surface pressures over the aileron results in a small moment about the aileron hinge. When the aileron is released at the start of an aeroelastic calculation, this unbalanced hinge moment deflects the aileron upwards and an unsteady oscillation begins. When the Mach number is increased slightly to $M = 0.8243$, this unsteady oscillation develops into a buzz limit cycle. Figure 12 shows the unsteady aileron deflection angle β versus time for $M = 0.8243$ during an aeroelastic calculation. As the figure shows, after three cycles of oscillation the aileron response settles into a limit cycle oscillation. The reduced frequency is $k = 0.3808$, which corresponds to a frequency of 21.67 Hz. This value compares well with the wind tunnel values that varied between 19.4 Hz and 21.2 Hz over a

variety of test conditions (ref. 29). The buzz frequency reported during the flight tests was 28 Hz (ref. 28). The calculated amplitude for the limit cycle oscillation is about $\pm 2°$ about an aileron uplift angle of $-1°$. In the wind tunnel tests and the Navier-Stokes calculations (refs. 29 and 3), the unsteady amplitude is about $\pm 10°$, and the value reported in the flight tests is 2° (ref. 28). This buzz calculation appears to represent the current limit of the inverse boundary-layer code as the calculation diverges when the Mach number is slightly increased.

Also, the calculated buzz conditions for this example changed slightly with the value of the time step used in the numerical integration. A summary of the variation observed for this example is presented in table III. The buzz Mach number varied from $M = 0.8241$ for $\Delta t = 0.02$ to $M = 0.8247$ for $\Delta t = 0.04$. The buzz frequency varied between 20.9 Hz for $\Delta t = 0.04$ and 21.7 Hz for $\Delta t = 0.01$. Although fully converged solutions were not obtained for this highly nonlinear case, the buzz phenomena persisted as the time step was decreased.

Figure 13 presents comparisons of buzz boundaries calculated by this method with the Navier-Stokes calculations of Steger and Bailey (ref. 3) and the wind tunnel experiments of reference 30. The CAP-TSD results were obtained for two values of the dynamic pressure: $q \approx 644$ psf, corresponding to sea level at standard atmospheric conditions, and $q \approx 293$ psf, corresponding to an altitude of 6096 m (20 000 ft). The time step for the CAP-TSD calculations was $\Delta t = 0.02$. As mentioned previously, the CAP-TSD results were obtained by releasing the aileron from its undeflected position and do not necessarily represent the minimum Mach number for the onset of buzz. For $q \approx 644$ psf, the buzz frequency was about 22 Hz for all cases. For $q \approx 293$ psf, the calculated buzz frequency was reduced to about 13 Hz. The Navier-Stokes result at $\alpha = -1°$ and $M = 0.83$ was obtained by releasing the aileron from its undeflected position, and this result is in reasonable agreement with the present calculations.

A CAP-TSD calculation that included three cycles of aeroelastic oscillations required less than 10 minutes of computer time on the Cray-2 computer at NASA Langley Research Center. Thus, the present technique offers an economical and reasonably accurate method for studying aileron buzz oscillations.

F-5 Wing

The CAP-TSD code with a stripwise viscous boundary layer has been applied to both steady and unsteady cases for the F-5 wing. The F-5 wing has a panel aspect ratio of 1.58, a leading-edge sweep angle of 31.9°, and a taper ratio of 0.28. The airfoil for this wing is a modified NACA 65A004.8 airfoil that has a drooped nose and is symmetrical aft of 40 percent chord. (See fig. 2(b).) The grid used for the F-5 calculations contains $137 \times 30 \times 84$ points in the x, y, and z directions. This grid extends ± 20 chords in the x and z directions and 2 semispans in the y direction, and it has 20 stations along the wing semispan with 55 points on each chord. The experimental data used in the comparisons are from reference 30.

Figure 14 presents comparisons of experimental and calculated pressure distributions for steady flow at a Mach number of 0.897 and $\alpha = -0.004°$. The inviscid calculations for the two inboard stations ($\eta_s = 0.181$ and 0.355) indicate a mild shock on the upper surface, whereas both the viscous calculation and the experiment show no evidence of a shock at these stations. The viscous calculation indicates the development of a shock at $\eta_s = 0.512$, and the experimental data suggest a mild shock at $\eta_s = 0.641$. All three results show a shock at the four outboard spanwise stations. The viscous shock is located about 2 percent upstream of the inviscid shock and generally is in better agreement with the experimental data, although the lack of experimental points makes the experimental location of the shock uncertain. Near the wing tip ($\eta_s = 0.977$), both the viscous and the inviscid calculations predict a shock location slightly upstream of the experimental results. The differences between calculated and experimental results near the wing tip may result from slight differences between the analytical model and the experimental wing in this region, highly three-dimensional flow effects near the wing tip, or coarseness of the grid used for the calculations.

Unsteady calculations were made for a Mach number of 0.899, $\alpha_0 = 0.002°$, $\alpha_1 = 0.109°$, and $k = 0.137$ ($f = 20$ Hz). (See figs. 15 and 16.) The time step used in the calculations corresponds to 500 steps per cycle of motion, and five cycles were calculated to allow for decay of any initial transients. The last cycle of the calculated results was Fourier analyzed to determine the harmonic content, and the first-harmonic components are compared with the experimental data in figures 15 and 16. The most noticeable feature of the upper surface unsteady pressures in figure 15 is the large variation in the calculated shock pulses near midchord. Although the viscous results are not always closer to the experimental data points in this region, the maximum amplitudes of the viscous results are substantially less than those of the inviscid results, and the viscous

shock pulses are slightly upstream of their inviscid counterparts. Hence, the viscous calculations are in better agreement with the data than the inviscid results. As also shown in figure 15, viscosity has little effect on the upper surface pressures upstream of the shock wave. Immediately downstream of the shock wave, the viscous results generally agree better with the experimental data than do the inviscid results. Near the trailing edge, essentially no difference occurs between the calculated viscous and inviscid unsteady pressures on the upper surface of the wing. Figure 16 indicates that on the lower surface of the wing the leading-edge suction peak is poorly predicted by both inviscid and viscous calculations. Away from the leading edge, the only significant differences between the viscous and inviscid unsteady calculations occur in the vicinity of midchord. In this region, the viscous results agree better with the experimental data than do the inviscid calculations. For the F-5 wing, the viscous results calculated with the interactive stripwise boundary layer provide a qualitative indication of the effects of viscosity within the cost-effective framework of transonic small-disturbance theory.

Conclusions

A method is presented for calculating turbulent viscous effects for two- and three-dimensional unsteady transonic flows, including flows involving mild separation. The method uses Green's lag-entrainment equations for attached turbulent flows and an inverse boundary-layer method developed by Melnik and Brook for separated turbulent flows. The inverse boundary-layer equations are coupled with the inviscid flow calculation through use of Carter's method. The viscous method uses steady boundary-layer equations in a quasi-steady manner, and the three-dimensional viscous effects are included in a stripwise fashion. The method has been applied to several two-dimensional test cases as well as a three-dimensional wing planform. The applications include the calculation of limit cycle oscillations, such as those that occur in aileron buzz. Comparisons are presented with experimental data and inviscid analyses as well as with another interactive boundary-layer method and Navier-Stokes calculations. The results demonstrate that accurate solutions are obtained for unsteady two-dimensional transonic flows with mild separation, and qualitative viscous effects are predicted for three-dimenisonal flow fields. The results have led to the following general conclusions:

1. For the NACA 64A010A airfoil, the lift coefficient calculated with the CAP-TSD viscous code shows a considerable improvement over previous calculations for the lower frequency AGARD cases. In particular, for the two lower frequencies, the imaginary part of the lift coefficient calculated with the CAP-TSD viscous code agrees well with the experimental data.

2. For the NACA 0012 airfoil, reasonably accurate calculations of lift and moment coefficients have been obtained with the viscous code for large-amplitude pitch oscillations, which are usually considered outside the range of transonic small-disturbance theory.

3. Instantaneous shock positions calculated with the viscous code during large-amplitude pitch oscillations of the NACA 0012 airfoil show better agreement with the experimental results than do those of the inviscid code.

4. The CAP-TSD viscous code accurately calculated the Mach number and frequency for the onset of aileron buzz for the airfoil on the P-80. The buzz boundary calculated with the viscous code agrees well with the experimental data and Navier-Stokes calculations.

5. The viscous code is relatively economical in terms of computer time. For example, an aeroelastic buzz calculation for three cycles of motion required less than 10 minutes computer time on a Cray-2.

6. For the F-5 wing, steady calculations with the viscous code predicted shock locations and strengths in better agreement with experimental results than did the inviscid calculations. Unsteady calculations indicate that the stripwise viscous boundary layer can provide a qualitative indication of viscous effects within the cost-effective framework of transonic small-disturbance theory.

7. The results presented demonstrate that the viscous solutions computed with the present algorithm can provide predictions of pressure distributions for unsteady transonic flow involving moderate-strength shock waves and mild flow separation that correlate better, sometimes significantly better, with experimental values than do the inviscid solutions.

NASA Langley Research Center
Hampton, VA 23665-5225
April 20, 1992

Appendix

Viscous Parameters for Attached Flow

For attached boundary layers, the various dependent variables and functions are evaluated from the following expressions.

$$\frac{U_e}{U} = 1 + \phi_x$$

$$\frac{M_e}{M} = 1 + \left(1 + \frac{\gamma - 1}{2} M^2\right) \phi_x$$

$$\frac{\rho_e}{\rho} = 1 - M^2 \phi_x$$

$$\frac{T_e}{T} = 1 - (\gamma - 1)\, M^2 \phi_x$$

The free-stream temperature in kelvins is T.

$$\frac{\mu_e}{\mu} = \left(\frac{T_e}{T}\right)^{3/2} \frac{1 + (N_{\mathrm{Su}}/T)}{(T_e/T) + (N_{\mathrm{Su}}/T)}$$

$$F = \frac{0.02 C_E + \frac{1.6}{1.2} C_E^2 + \frac{0.8 C_{f_o}}{3}}{0.01 + \frac{1.6}{1.2} C_E}$$

$$C_\tau = \left(1 + 0.1 M_e^2\right) \left(0.024 C_E + 1.6 C_E^2 + 0.32 C_{f_o}\right)$$

$$\lambda = \begin{cases} 1 & \text{(On airfoil)} \\ 1/2 & \text{(On wake)} \end{cases}$$

$$\left(\frac{\theta}{U_e} \frac{dU_e}{dx}\right)_{\mathrm{EQO}} = \frac{1.25}{H} \left[\frac{C_f}{2} - \left(\frac{\overline{H} - 1}{6.432 \overline{H}}\right)^2 \left(1 + 0.04 M_e^2\right)^{-1}\right]$$

$$(C_E)_{\mathrm{EQO}} = H_1 \left[\frac{C_f}{2} - (H + 1) \left(\frac{\theta}{U_e} \frac{dU_e}{dx}\right)_{\mathrm{EQO}}\right]$$

$$(C_\tau)_{\mathrm{EQO}} = \left(1 + 0.1 M_e^2\right) \times \left[0.024 (C_E)_{\mathrm{EQO}} + 1.6 (C_E)_{\mathrm{EQO}}^2 + 0.32 C_{f_o}\right]$$

$$N_{\mathrm{Re},\theta} = \frac{(\rho_e/\rho)\,(U_e/U)\,(\theta)}{\mu_e/\mu} N_{\mathrm{Re}}$$

$$r = N_{\mathrm{Pr},t}^{1/3}$$

$$F_c = \left(1 + \frac{\gamma - 1}{2} r M_e^2\right)^{1/2}$$

$$F_r = 1 + 0.056 M_e^2$$

$$C_{f_o} = \frac{1}{F_c} \left[\frac{0.01013}{\log_{10}\left(F_r N_{\mathrm{Re},\theta}\right) - 1.02} - 0.00075\right]$$

$$\frac{\overline{H}}{\overline{H}_o} = \overline{H} \left\{1 - 6.55 \left[\frac{C_{f_o}}{2} \left(1 + 0.04 M_e^2\right)\right]^{1/2}\right\}$$

$$C_f = \begin{cases} C_{f_o} \left[0.9 \left(\frac{\overline{H}}{\overline{H}_o} - 0.4\right)^{-1} - 0.5\right] & \text{(On airfoil)} \\ 0 & \text{(On wake)} \end{cases}$$

$$H = (\overline{H} + 1) \left(1 + \frac{\gamma - 1}{2} r M_e^2\right) - 1$$

$$H_1 = 3.15 + \frac{1.72}{\overline{H} - 1} - 0.01 (\overline{H} - 1)^2$$

$$\frac{d\overline{H}}{dH_1} = \frac{-(\overline{H} - 1)^2}{1.72 + 0.02 (\overline{H} - 1)^3}$$

$$C = (C_\tau)_{\mathrm{EQO}} \left(1 + 0.1 M_e^2\right)^{-1} \lambda^{-2} - 0.32 C_{f_o}$$

$$(C_E)_{\mathrm{EQ}} = \left(\frac{C}{1.6} + 0.0001\right)^{1/2} - 0.01$$

$$\left(\frac{\theta}{U_e}\frac{dU_e}{dx}\right)_{\mathrm{EQ}} = \left[\frac{1}{H_1\,(H+1)}\right]\left[\frac{H_1 C_f}{2} - (C_E)_{\mathrm{EQ}}\right]$$

The additional parameters required to specify the boundary-layer equations completely, together with the default values in the code (in parentheses), are the free-stream chord Reynolds number $N_{\mathrm{Re}}\left(10^7\right)$, the free-stream temperature T in kelvins (300 K), the turbulent Prandtl number $N_{\mathrm{Pr},t}$ (0.9 for air), and the Sutherland law viscosity constant N_{Su} in kelvins (110 K for air).

References

1. Edwards, John W.; and Thomas, James L.: Computational Methods for Unsteady Transonic Flows. AIAA-87-0107, Jan. 1987.

2. Malone, J. B.; Sankar, L. N.; and Sotomayer, W. A.: Unsteady Aerodynamic Modeling of a Fighter Wing in Transonic Flow. *J. Aircr.*, vol. 23, no. 7, July 1986, pp. 611–620.

3. Steger, J. L.; and Bailey, H. E.: Calculation of Transonic Aileron Buzz. *AIAA J.*, vol. 18, no. 3, Mar. 1980, pp. 249–255.

4. Anderson, W. Kyle; and Batina, John T.: Accurate Solutions, Parameter Studies, and Comparisons for the Euler and Potential Flow Equations. *Validation of Computational Fluid Dynamics, Volume 1 Symposium Papers*, AGARD-CP-437 Vol. I, Dec. 1988, pp. 14-1–14-16. (Available as NASA TM-100664, 1988.)

5. Batina, John T.; Seidel, David A.; Bland, Samuel R.; and Bennett, Robert M.: Unsteady Transonic Flow Calculations for Realistic Aircraft Configurations. *J. Aircr.*, vol. 26, no. 1, Jan. 1989, pp. 21–28.

6. Batina, John T.: Unsteady Transonic Algorithm Improvements for Realistic Aircraft Applications. *J. Aircr.*, vol. 26, no. 2, Feb. 1989, pp. 131–139.

7. Bland, Samuel R.; and Seidel, David A.: *Calculation of Unsteady Aerodynamics for Four AGARD Standard Aeroelastic Configurations.* NASA TM-85817, 1984.

8. Bennett, Robert M.; and Batina, John T.: Application of the CAP-TSD Unsteady Transonic Small Disturbance Program to Wing Flutter. *Proceedings—European Forum on Aeroelasticity and Structural Dynamics 1989*, DGLR-Bericht 89-01, Deutsche Gesellschaft fur Luft- und Raumfahrt e.V., 1989, pp. 25–34.

9. Batina, John T.: Unsteady Transonic Flow Calculations for Interfering Lifting Surface Configurations. *J. Aircr.*, vol. 23, no. 5, May 1986, pp. 422–430.

10. Melnik, R. E.; Chow, R. R.; Mead, H. R.; and Jameson, A.: *An Improved Viscid/Inviscid Interaction Procedure for Transonic Flow Over Airfoils.* NASA CR-3805, 1985.

11. Houwink, R.: *Results of a New Version of the LTRAN2-NLR Code (LTRANV) for Unsteady Viscous Transonic Flow Computations.* NLR TR 81078 U, National Aerospace Lab. NLR (Amsterdam, Netherlands), July 7, 1981.

12. Rizzetta, Donald P.: *Procedures for the Computation of Unsteady Transonic Flows Including Viscous Effects.* NASA CR-166249, 1982.

13. Streett, Craig L.: Viscous-Inviscid Interaction for Transonic Wing-Body Configurations Including Wake Effects. *AIAA J.*, vol. 20, no. 7, July 1982, pp. 915–923.

14. Howlett, James T.; and Bland, Samuel R.: *Calculation of Viscous Effects on Transonic Flow for Oscillating Airfoils and Comparisons With Experiment.* NASA TP-2731, 1987.

15. Le Balleur, J. C.: Strong Matching Method for Computing Transonic Viscous Flows Including Wakes and Separations Lifting Airfoils. *Recherche Aerosp.* (English Edition), no. 3, 1981, pp. 21–45.

16. LeBalleur, J. C.; and Girodroux-Lavigne, P.: A Viscous-Inviscid Interaction Method for Computing Unsteady Transonic Separation. *Third Symposium on Numerical and Physical Aspects of Aerodynamic Flows*, California State Univ., Jan. 1985, pp. 5–49.

17. Melnik, R. E.; and Brook, J. W.: The Computation of Viscid/Inviscid Interaction on Airfoils With Separated Flow. *Third Symposium on Numerical and Physical Aspects of Aerodynamic Flows*, California State Univ., 1985, pp. 1-21–1-37.

18. Batina, John T.: Efficient Algorithm for Solution of the Unsteady Transonic Small-Disturbance Equation. *J. Aircr.*, vol. 25, no. 7, July 1988, pp. 598–605.

19. Batina, John T.: Unsteady Transonic Small-Disturbance Theory Including Entropy and Vorticity Effects. *J. Aircr.*, vol. 26, no. 6, June 1989, pp. 531–538.

20. Carter, James E.: A New Boundary-Layer Inviscid Iteration Technique for Separated Flow. *A Collection of Technical Papers—Computational Fluid Dynamics Conference*, American Inst. of Aeronautics and Astronautics, Inc., July 1979, pp. 45–55. (Available as AIAA Paper No. 79-1450.)

21. Cunningham, Herbert J.; Batina, John T.; and Bennett, Robert M.: Modern Wing Flutter Analysis by Computational Fluid Dynamics Methods. *J. Aircr.*, vol. 25, no. 10, Oct. 1988, pp. 962–968.

22. Bennett, Robert M.; Bland, Samuel R.; Batina, John T.; Gibbons, Michael D.; and Mabey, Dennis G.: Calculation of Steady and Unsteady Pressures on Wings at Supersonic Speeds With a Transonic Small Disturbance Code. *A Collection of Technical Papers AIAA/ASME/ASCE/AHS 28th Structures, Structural Dynamics and Materials Conference and AIAA Dynamics Specialists Conference, Part 2A*, American Inst. of Aeronautics and Astronautics, Inc., Apr. 1987, pp. 363–377. (Available as AIAA-87-0851.)

23. Whitlow, Woodrow, Jr.: *Characteristic Boundary Conditions for Three-Dimensional Transonic Unsteady Aerodynamics.* NASA TM-86292, 1984.

24. Green, J. E.; Weeks, D. J.; and Brooman, J. W. F.: *Prediction of Turbulent Boundary Layers and Wakes in Compressible Flow by a Lag-Entrainment Method.* R. & M. No. 3791, British Aeronautical Research Council, 1977.

25. Thomas, James Lee: Transonic Viscous-Inviscid Interaction Using Euler and Inverse Boundary-Layer Equations. Ph.D. Diss., Mississippi State Univ., Dec. 1983.

26. Davis, Sanford S.; and Malcolm, Gerald H.: *Experimental Unsteady Aerodynamics of Conventional and Supercritical Airfoils.* NASA TM-81221, 1980.

27. Landon, R. H.: NACA 0012. Oscillatory and Transient Pitching. *Compendium of Unsteady Aerodynamic Measurements*, AGARD-R-702, Aug. 1982, pp. 3-1–3-25.
28. Brown, Harvey H.; Rathert, George A., Jr.; and Clousing, Lawrence A.: *Flight-Test Measurements of Aileron Control Surface Behaviour at Supercritical Mach Numbers.* NACA RM A7A15, 1947.
29. Erickson, Albert L.; and Stephenson, Jack D.: *A Suggested Method of Analyzing for Transonic Flutter of Control Surfaces Based on Available Experimental Evidence.* NACA RM A7F30, 1947.
30. Tijdeman, H.; Van Nunen, J. W. G.; Kraan, A. N.; Persoon, A. J.; Poestkoke, R.; Roos, R.; Schippers, P.; and Siebert, C. M.: *Transonic Wind Tunnel Tests on an Oscillating Wing With External Stores.* AFFDL-TR-78-194, U.S. Air Force.
Part I—General Description, Dec. 1978.
Part II—The Clean Wing, Mar. 1979.
Part III The Wing With Tip Store, May 1979.
Part IV—The Wing With Underwing-Store, Sept. 1979.
(Available from DTIC as AD A077 370.)

Table I. Analytical Test Cases for NACA 64A010A Airfoil

$[M = 0.796;\ N_{\mathrm{Re}} = 12.5 \times 10^6;\ \alpha_0 = 0°;\ x_a/c = 0.25]$

Case	α_1, deg	f, Hz	k
3	1.03	4.2	0.025
4	1.02	8.6	.051
5	1.02	17.2	.101
6	1.01	34.4	.202
7	.99	51.5	.303

Table II. Analytical Test Cases for NACA 0012 Airfoil

$[k = 0.081;\ x_a/c = 0.25]$

Case	M	U, m/sec	N_{Re}	α_0, deg	α_1, deg	f, Hz
1	0.601	197	4.8×10^6	2.89	2.41	50
2	.599	197	4.8	3.16	4.59	50
3	.599	197	4.8	4.86	2.44	50
5	.755	243	5.5	.02	2.51	62

Table III. Variation of Buzz Conditions With Time Step at $\alpha = 0°$

Time step	Steps per cycle	M_B	q_B, psi	k_B	f_B, Hz
0.04	214	0.8247	644.9	0.367	20.9
.02	422	.8241	644.3	.372	21.2
.01	825	.8243	644.5	.381	21.7

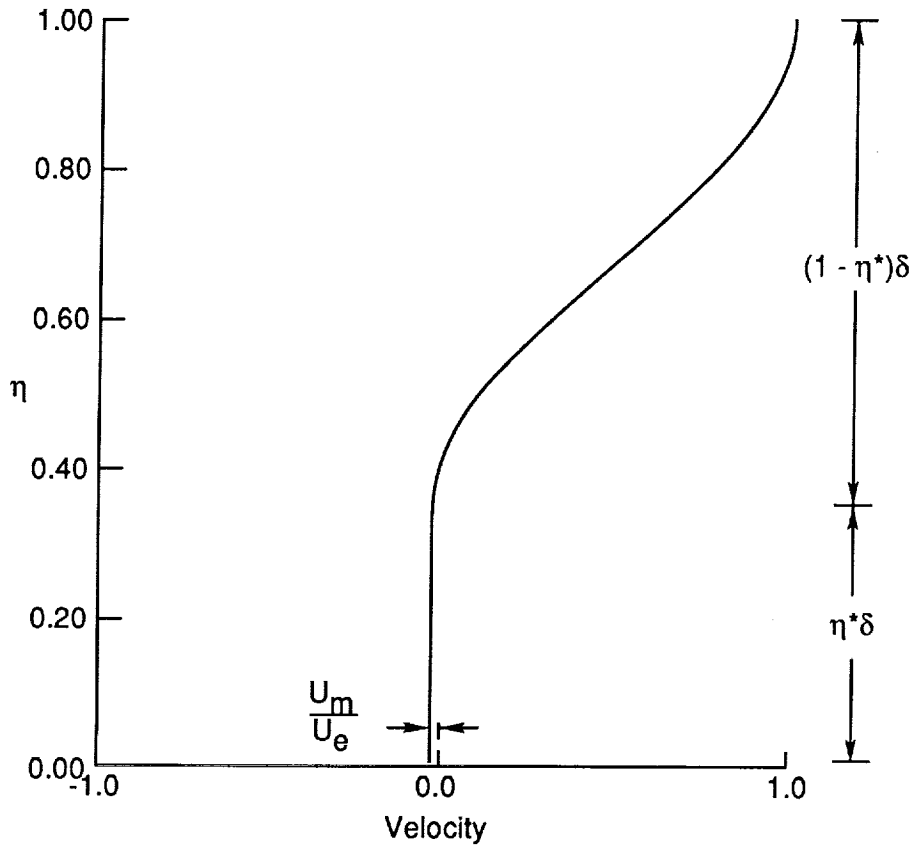

Figure 1. Velocity profile for inverse boundary-layer analysis. $\overline{H} = 10.0$.

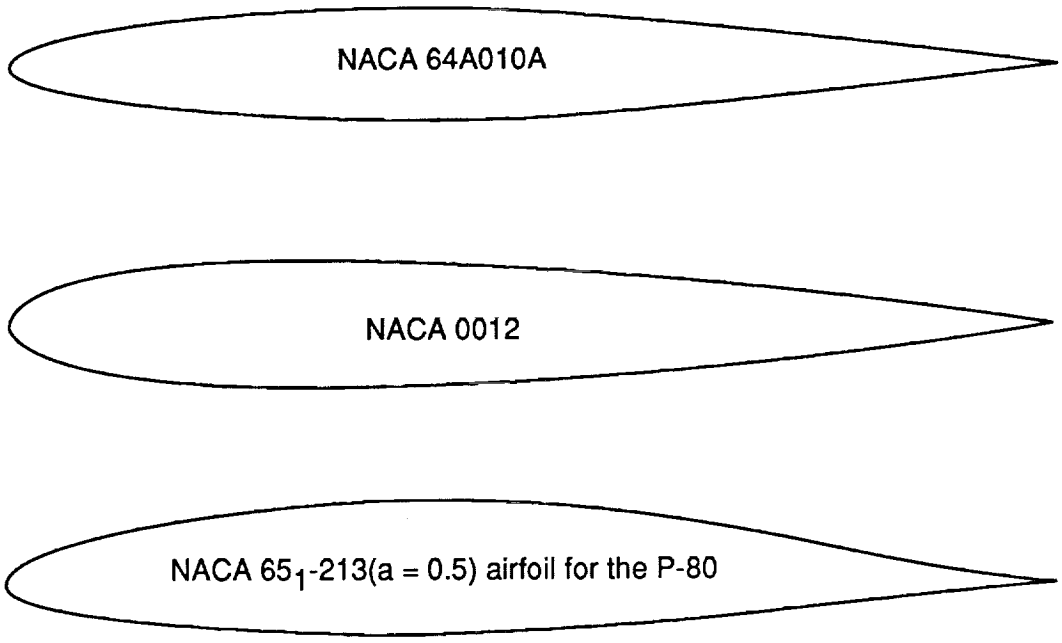

(a) Two-dimensional airfoils.

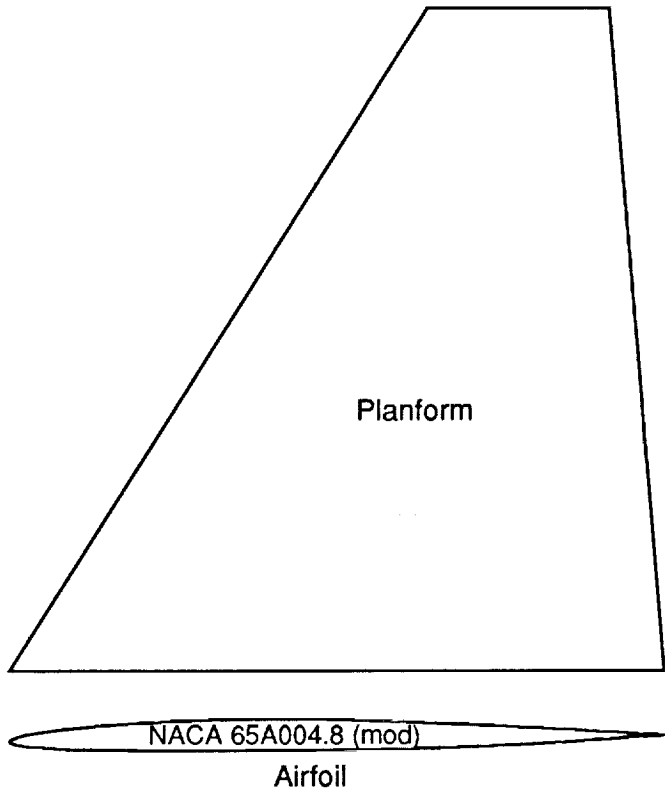

(b) F-5 wing.

Figure 2. Configurations studied.

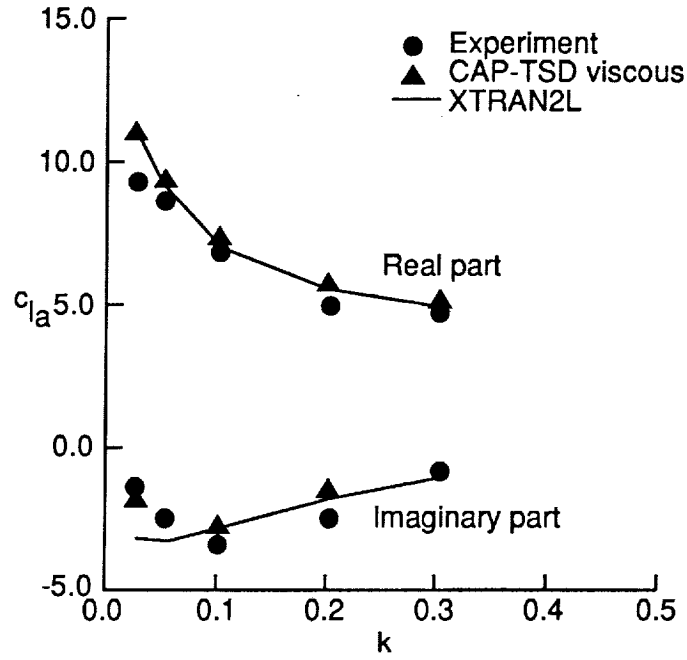

Figure 3. Comparison of unsteady lift coefficient for the NACA 64A010A airfoil. $M = 0.796$; $\alpha_1 = 1°$.

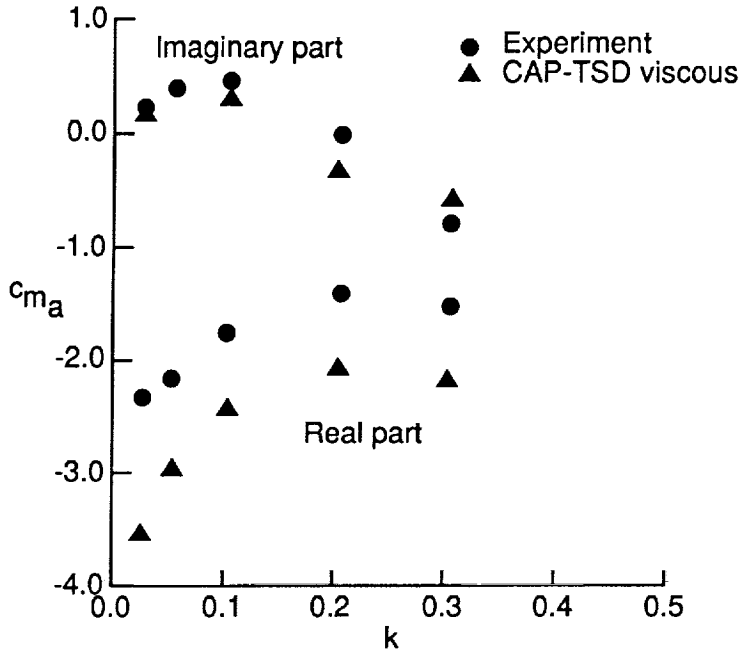

Figure 4. Comparison of unsteady pitching-moment coefficient for the NACA 64A010A airfoil. $M = 0.796$; $\alpha_1 = 1°$.

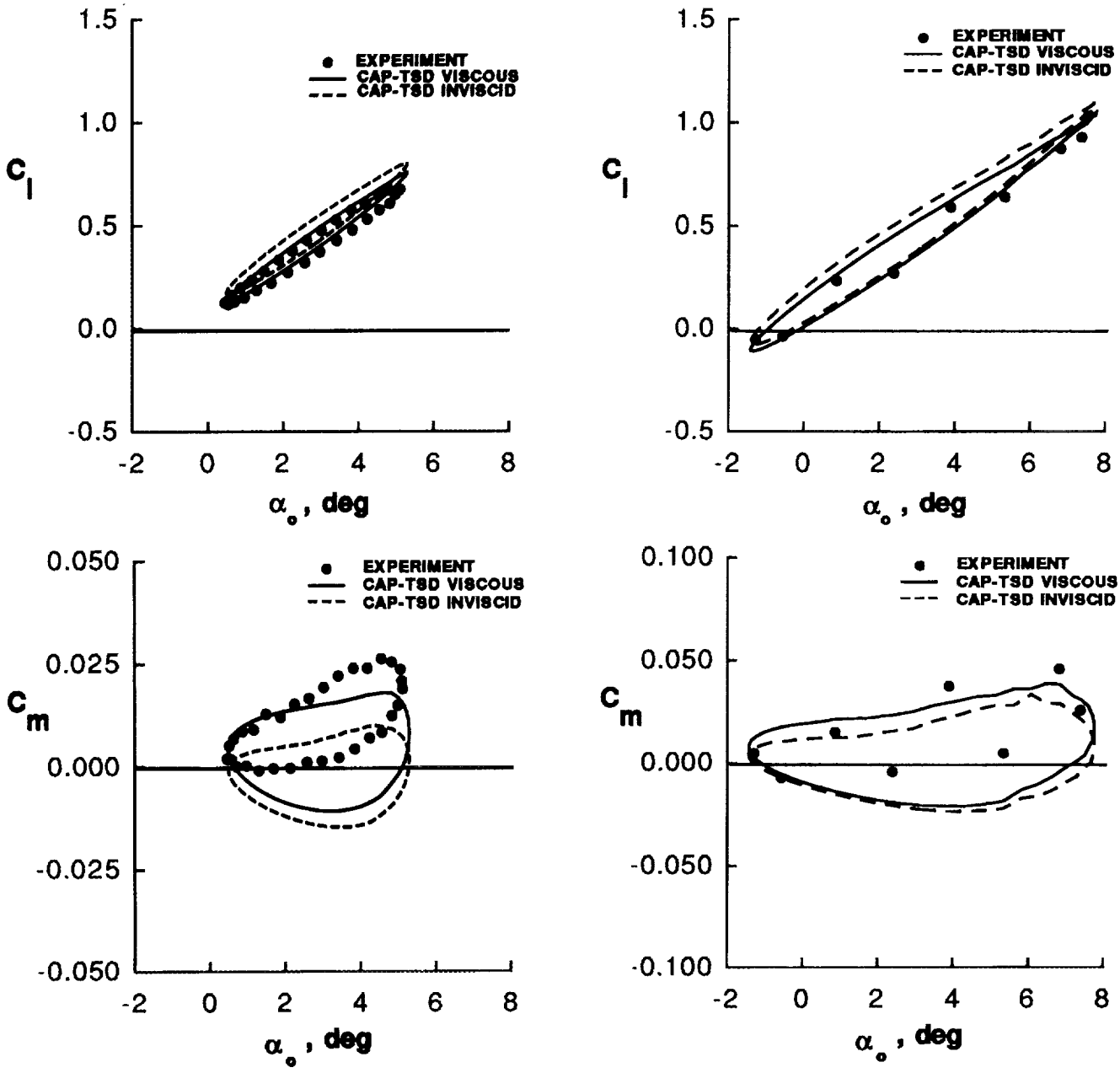

(a) Case 1. $M = 0.601$; $\alpha_0 = 2.89°$; $\alpha_1 = 2.41°$; $N_{\mathrm{Re}} = 4.8 \times 10^6$.

(b) Case 2. $M = 0.599$; $\alpha_0 = 3.16°$; $\alpha_1 = 4.59°$; $N_{\mathrm{Re}} = 4.8 \times 10^6$.

Figure 5. Comparison of unsteady forces versus angle of attack for cases 1, 2, 3, and 5 for the NACA 0012 airfoil at $k = 0.081$.

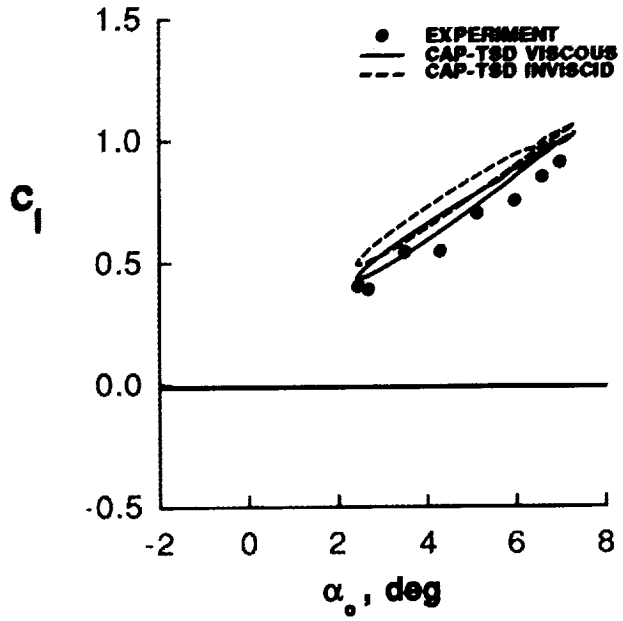

(c) Case 3. $M = 0.599$; $\alpha_0 = 4.86°$; $\alpha_1 = 2.44°$; $N_{\mathrm{Re}} = 4.8 \times 10^6$.

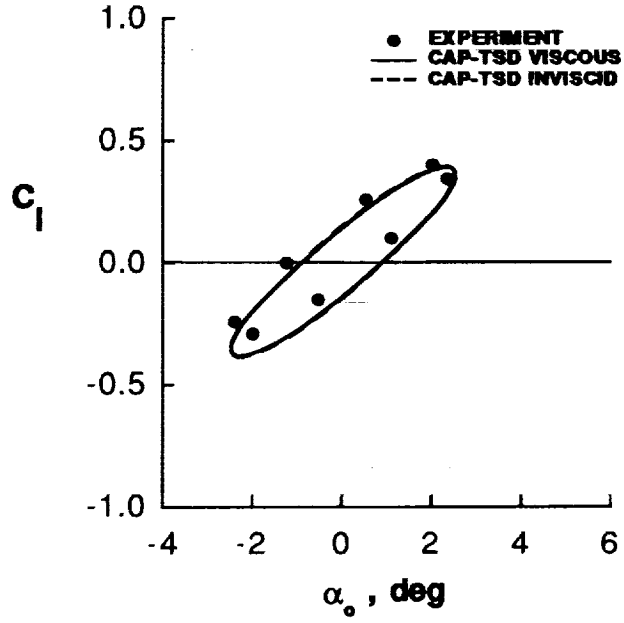

(d) Case 5. $M = 0.755$; $\alpha_0 = 0.02°$; $\alpha_1 = 2.51°$; $N_{\mathrm{Re}} = 5.5 \times 10^6$.

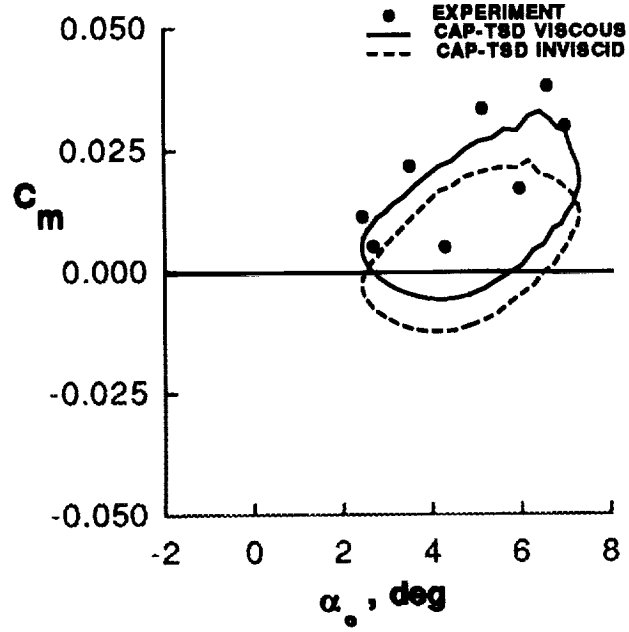

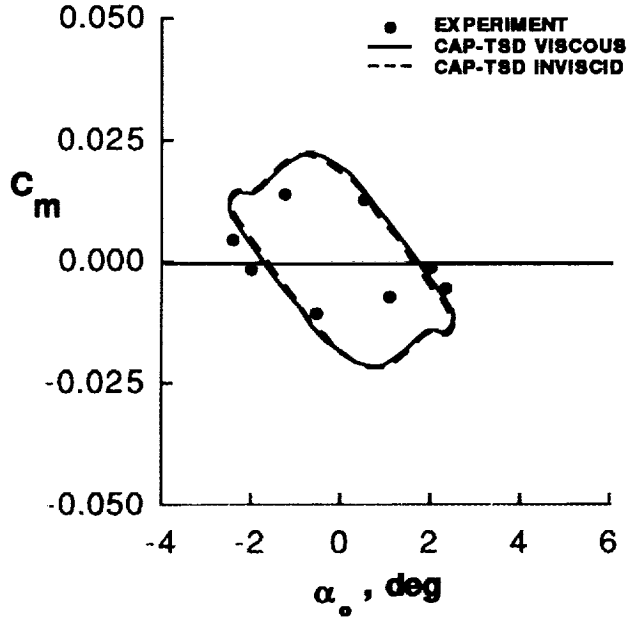

Figure 5. Concluded.

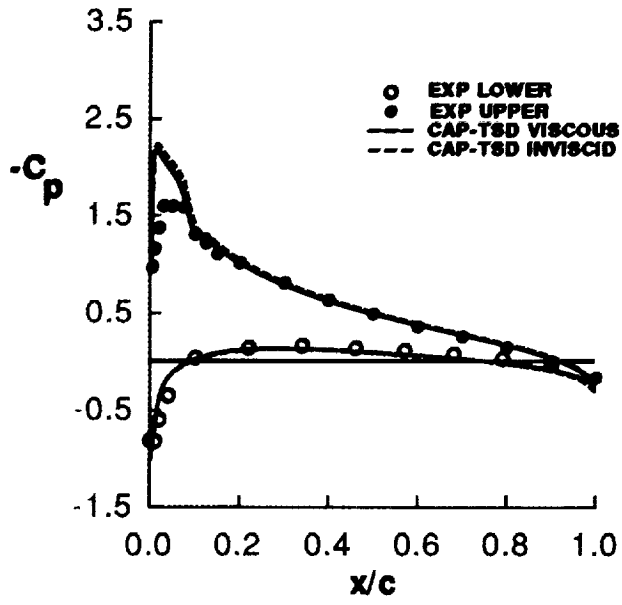

(a) $\alpha = 4.23° \uparrow$.

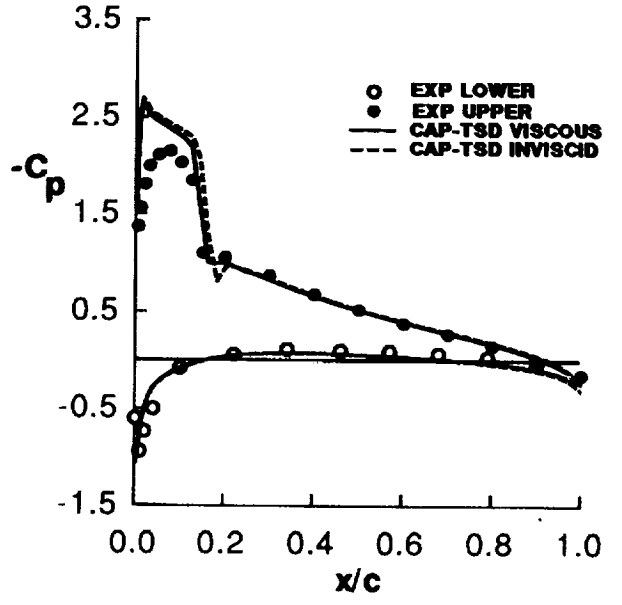

(b) $\alpha = 5.11° \uparrow$.

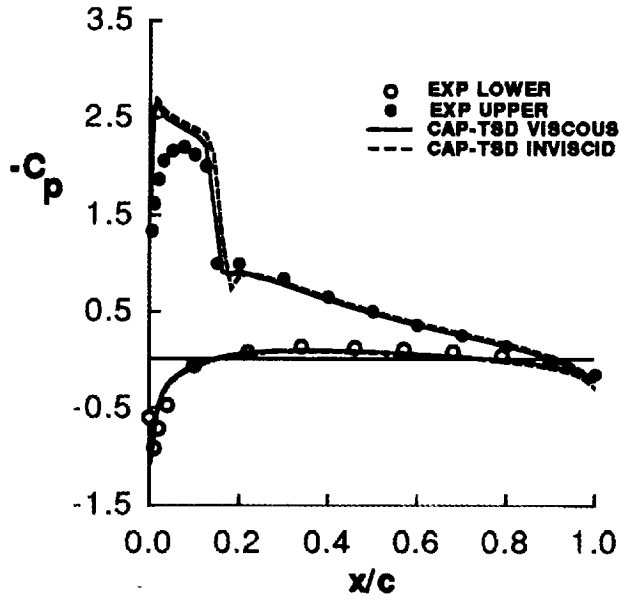

(c) $\alpha = 4.54° \downarrow$.

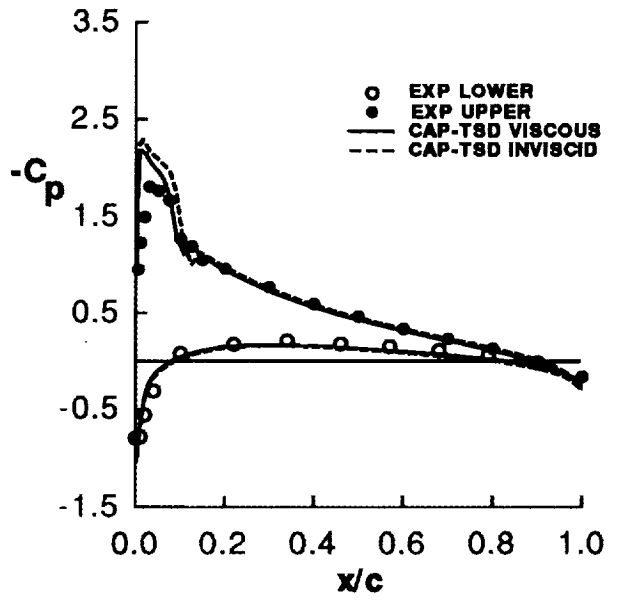

(d) $\alpha = 3.01° \downarrow$.

Figure 6. Comparison of instantaneous unsteady pressures for case 1 for the NACA 0012 airfoil. $M = 0.601$; $\alpha_0 = 2.89°$; $\alpha_1 = 2.41°$; $k = 0.081$; $N_{\mathrm{Re}} = 4.8 \times 10^6$.

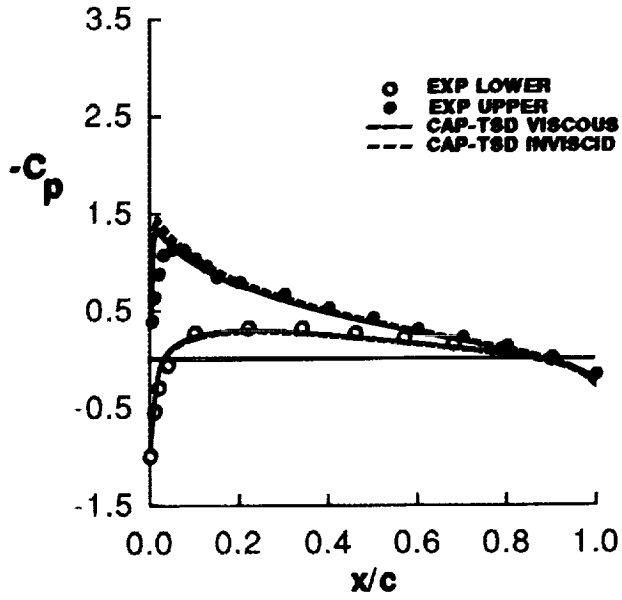

(e) $\alpha = 1.48°\downarrow$.

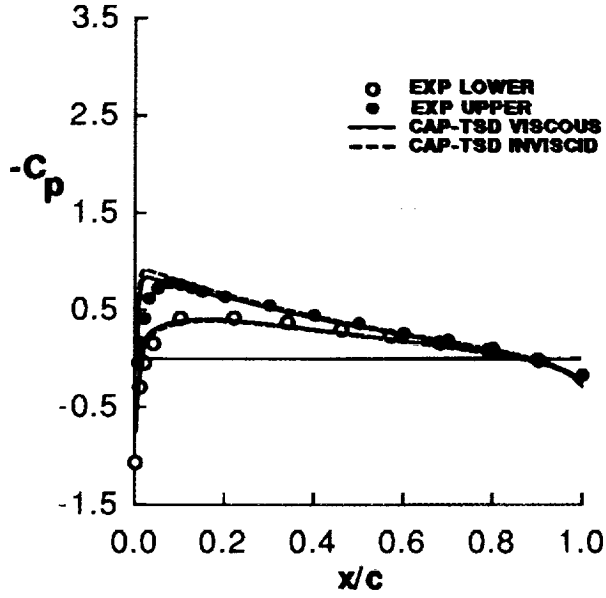

(f) $\alpha = 0.50°\downarrow$.

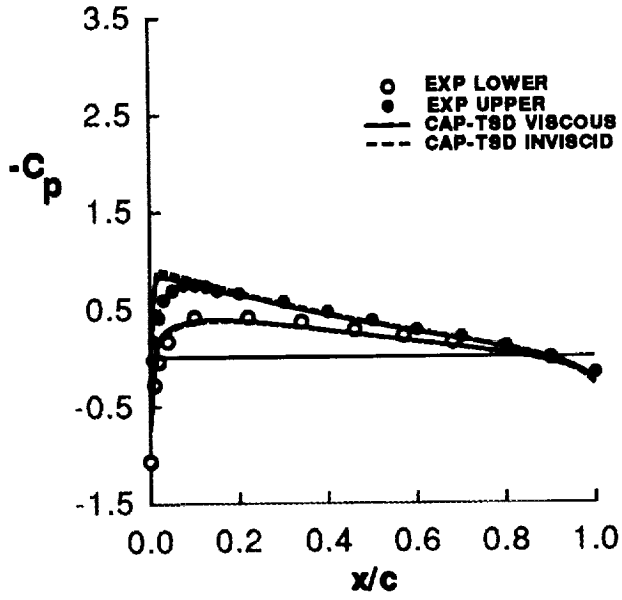

(g) $\alpha = 0.96°\uparrow$.

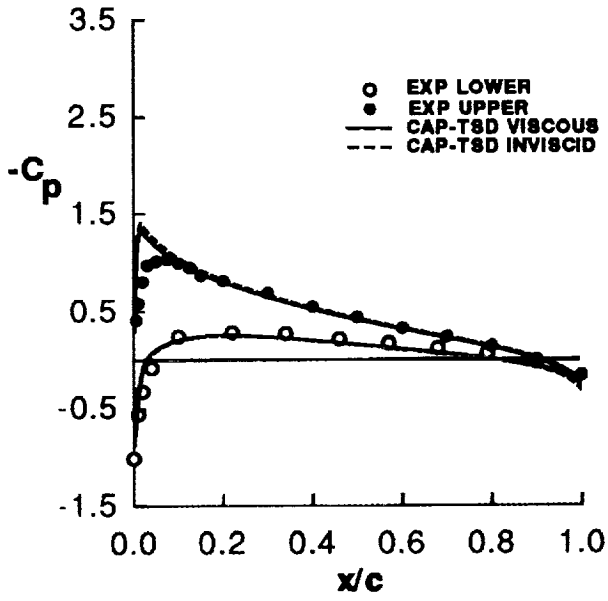

(h) $\alpha = 2.57°\uparrow$.

Figure 6. Concluded.

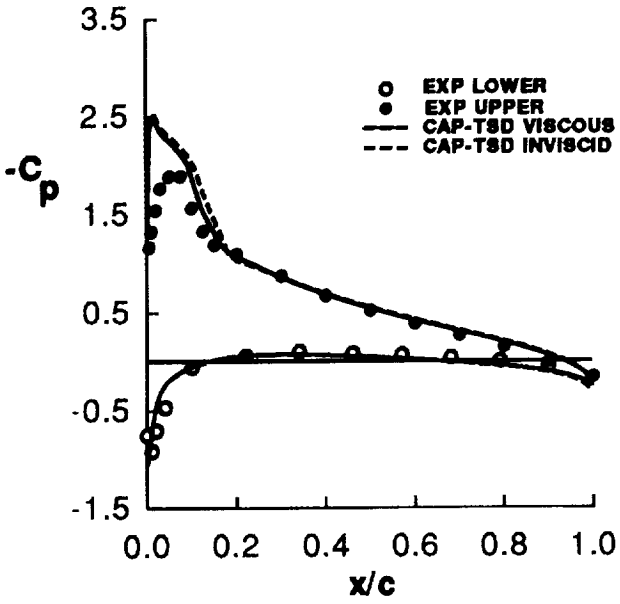

(a) $\alpha = 5.32° \uparrow$.

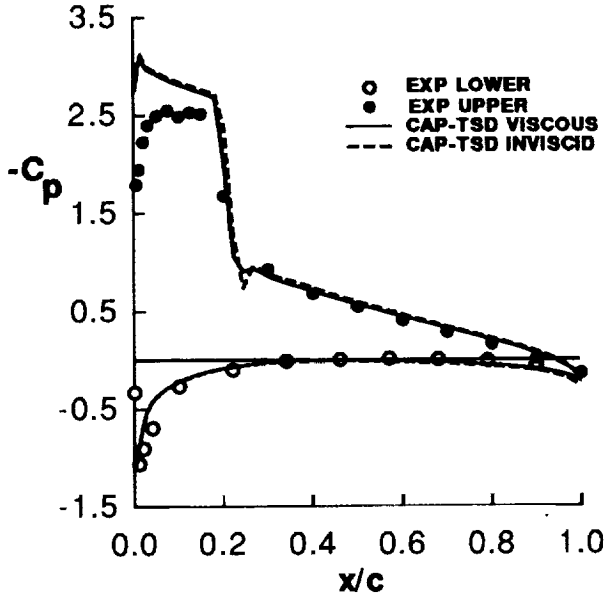

(b) $\alpha = 7.36° \uparrow$.

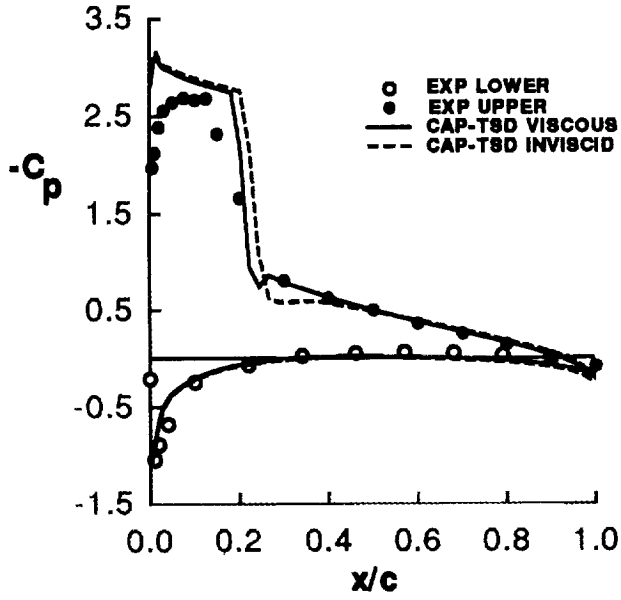

(c) $\alpha = 6.80° \downarrow$.

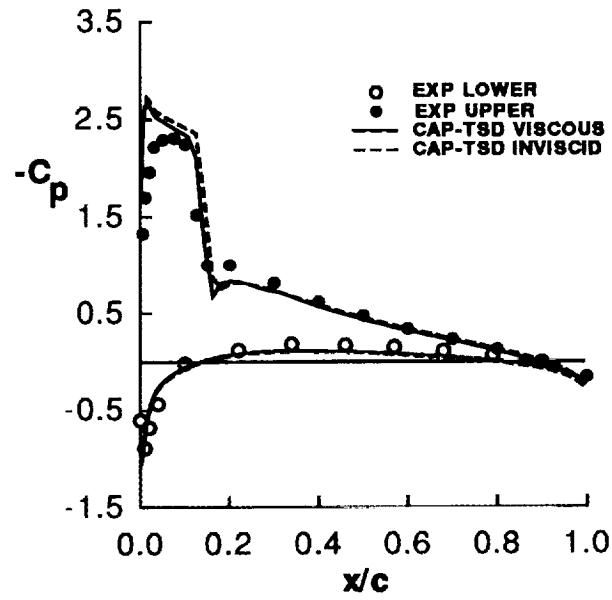

(d) $\alpha = 3.88° \downarrow$.

Figure 7. Comparison of instantaneous unsteady pressures for case 2 for the NACA 0012 airfoil. $M = 0.599$; $\alpha_0 = 3.16°$; $\alpha_1 = 4.59°$; $k = 0.081$; $N_{\mathrm{Re}} = 4.8 \times 10^6$.

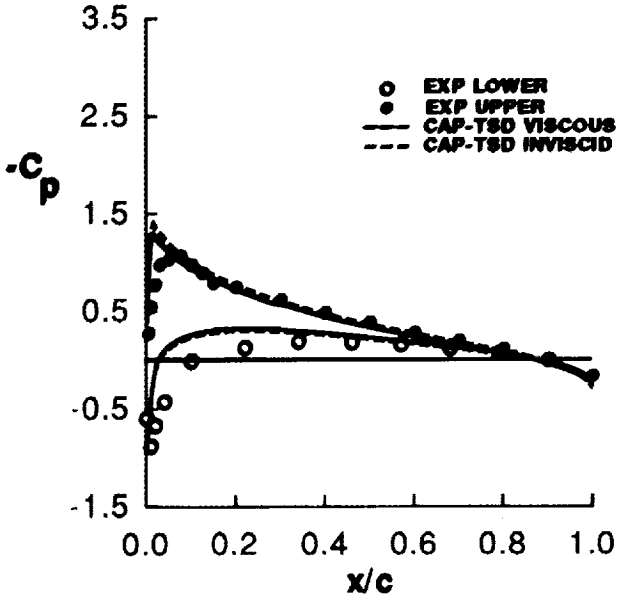

(c) $\alpha = 0.86°$ ↓.

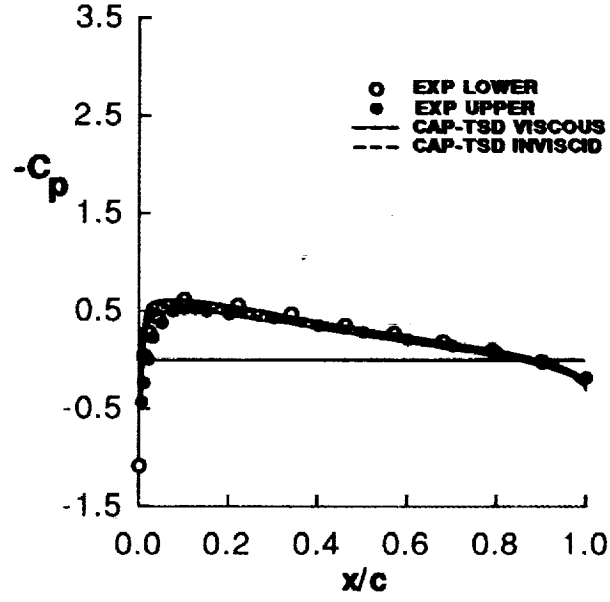

(f) $\alpha = -1.30°$ ↓.

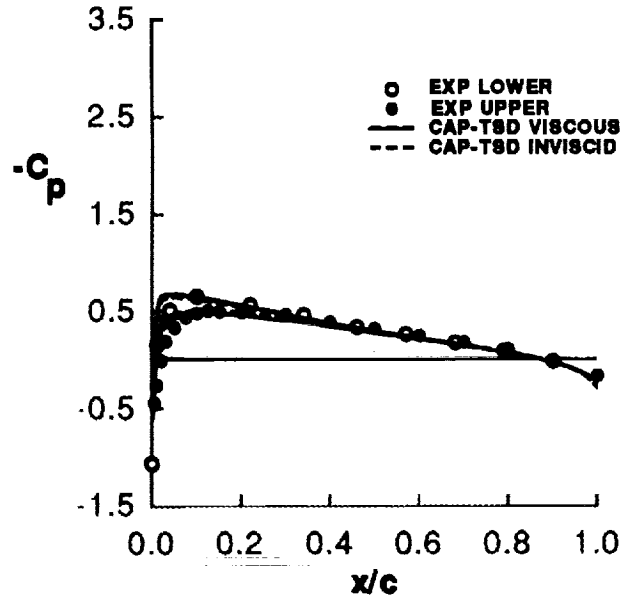

(g) $\alpha = -0.57°$ ↑.

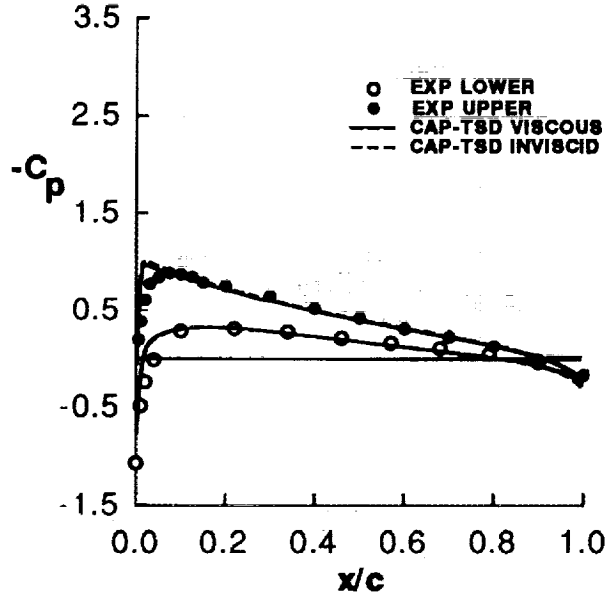

(h) $\alpha = 2.38°$ ↑.

Figure 7. Concluded.

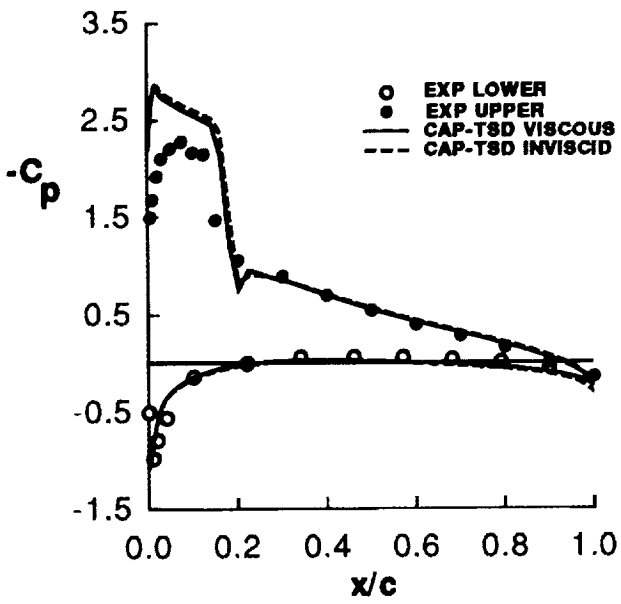

(a) $\alpha = 5.95°$ ↑.

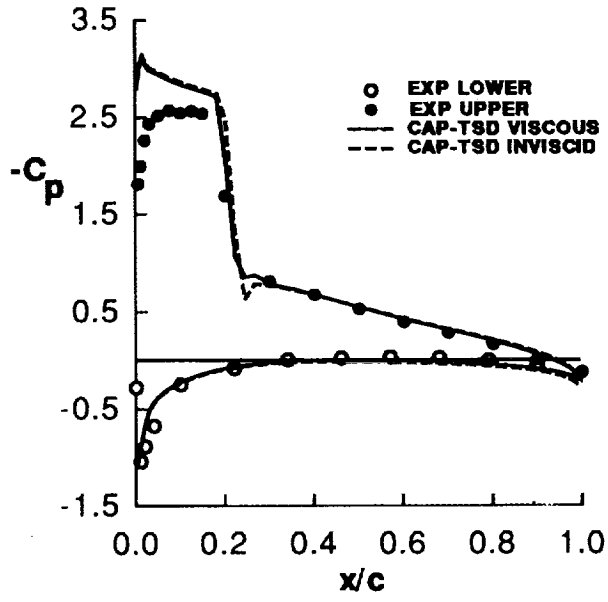

(b) $\alpha = 6.97°$ ↑.

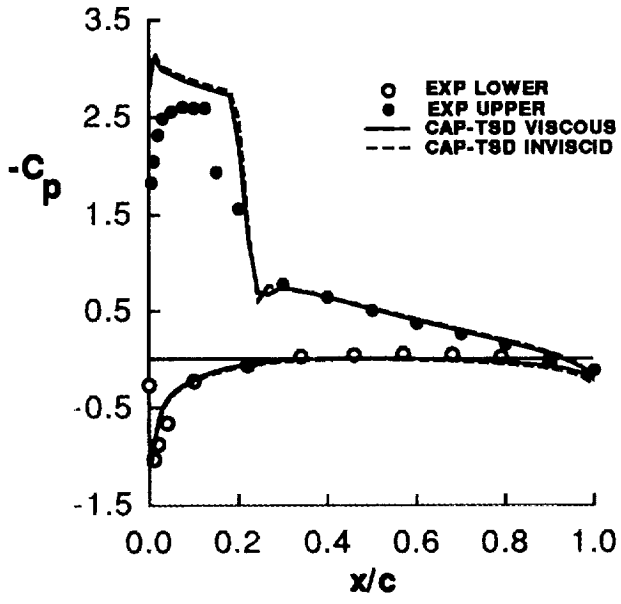

(c) $\alpha = 6.57°$ ↓.

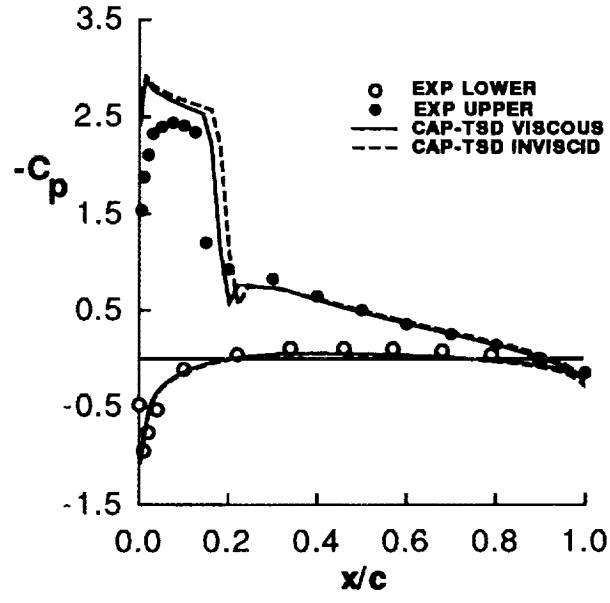

(d) $\alpha = 5.11°$ ↓.

Figure 8. Comparison of instantaneous unsteady pressures for case 3 for the NACA 0012 airfoil. $M = 0.599$; $\alpha_0 = 4.86°$; $\alpha_1 = 2.44°$; $k = 0.081$; $N_{\mathrm{Re}} = 4.8 \times 10^6$.

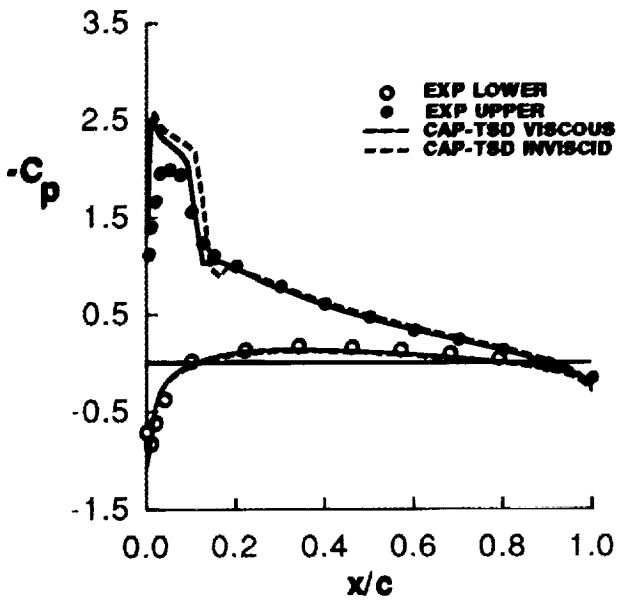

(e) $\alpha = 3.49° \downarrow$.

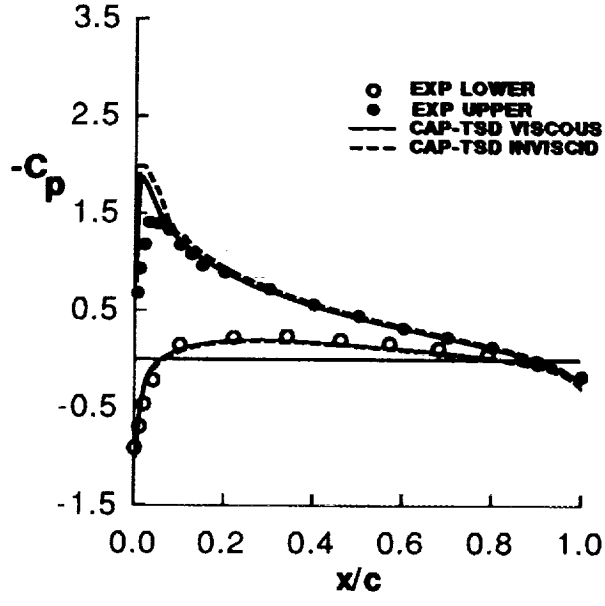

(f) $\alpha = 2.43° \downarrow$.

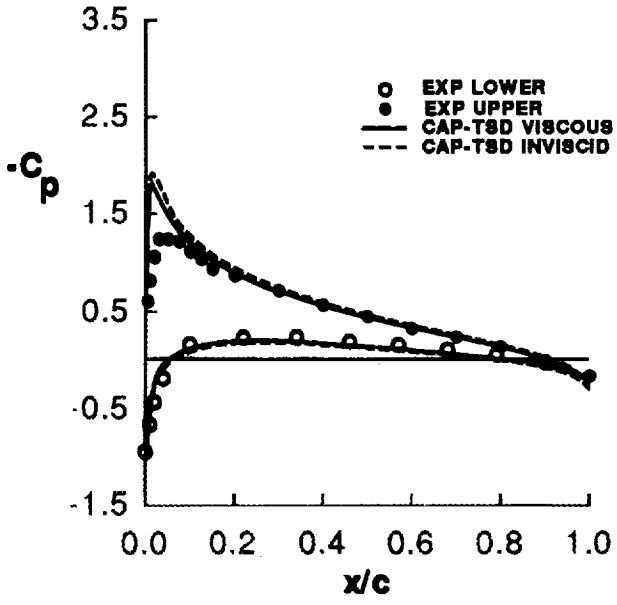

(g) $\alpha = 2.67° \uparrow$.

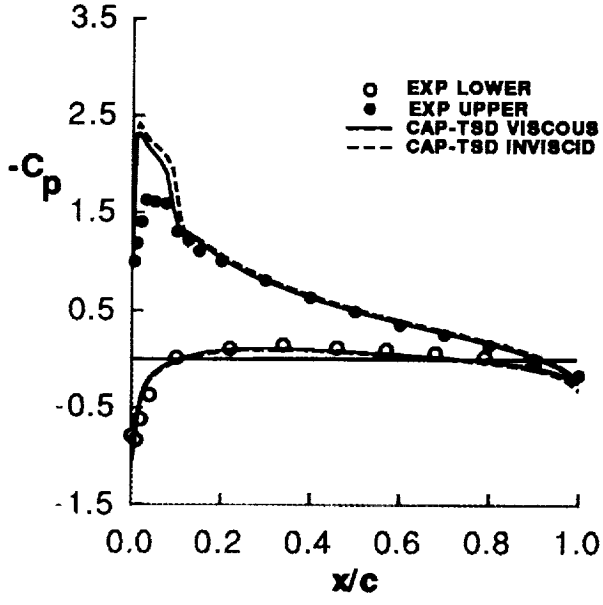

(h) $\alpha = 4.28° \uparrow$.

Figure 8. Concluded.

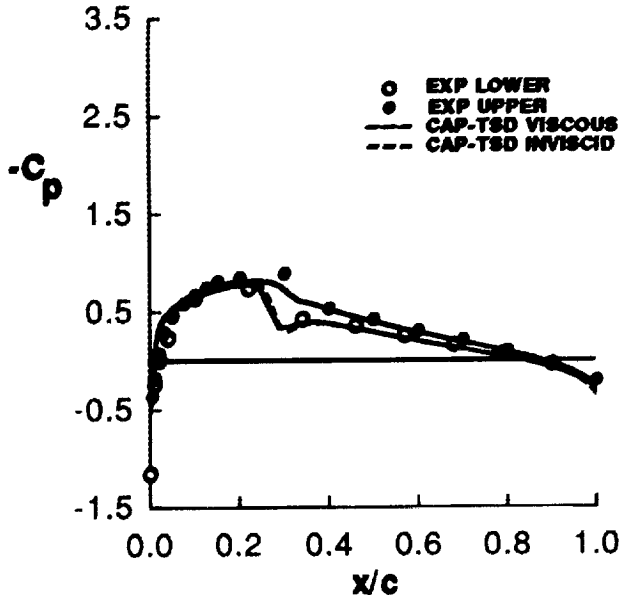

(a) $\alpha = 1.09°\uparrow$.

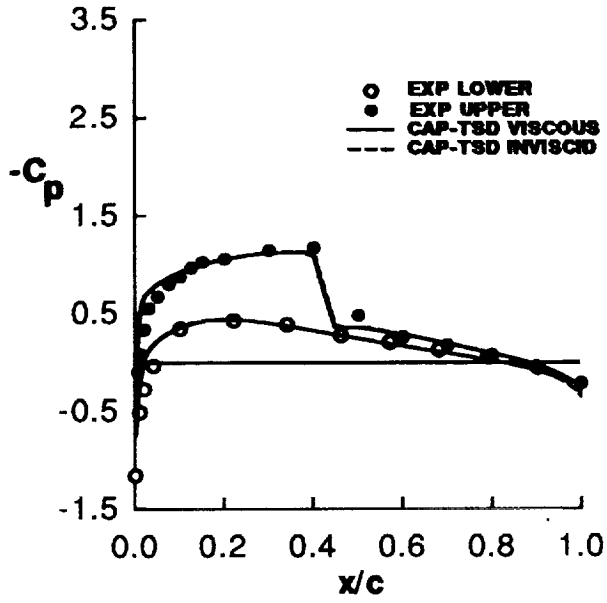

(b) $\alpha = 2.34°\uparrow$.

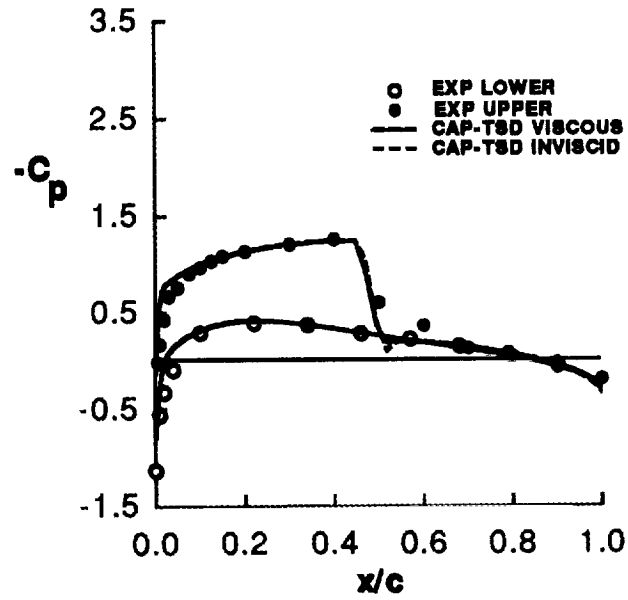

(c) $\alpha = 2.01°\downarrow$.

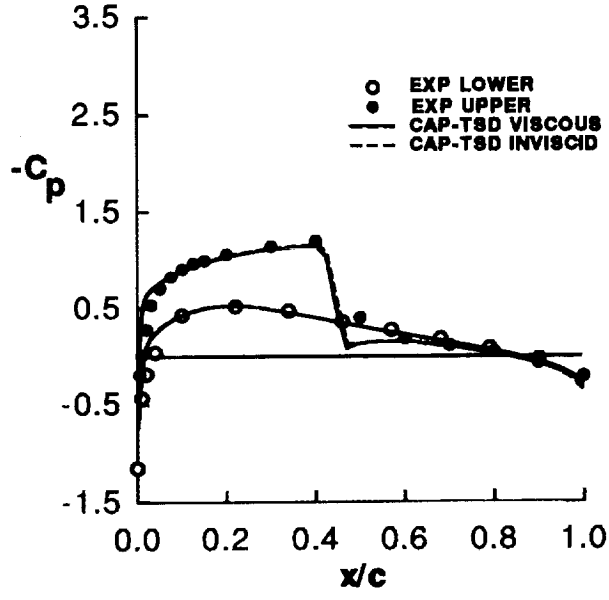

(d) $\alpha = 0.52°\downarrow$.

Figure 9. Comparison of instantaneous unsteady pressures for case 5 for the NACA 0012 airfoil. $M = 0.755$; $\alpha_0 = 0.02°$; $\alpha_1 = 2.51°$; $k = 0.081$; $N_{\mathrm{Re}} = 5.5 \times 10^6$.

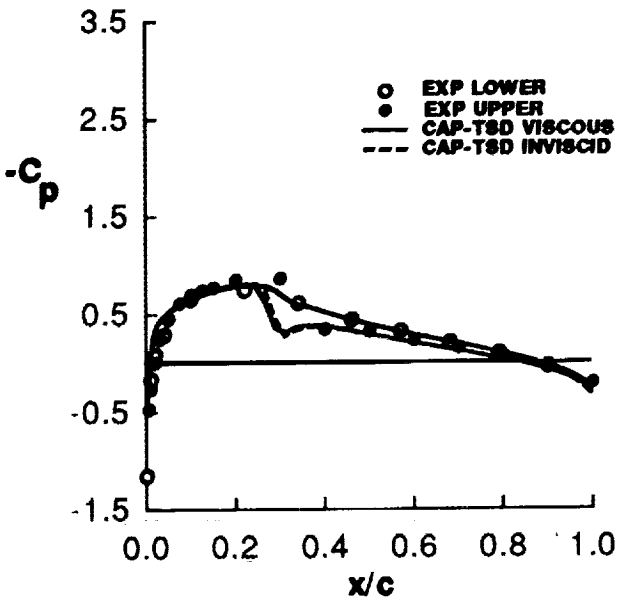

(e) $\alpha = -1.25°$ ↓.

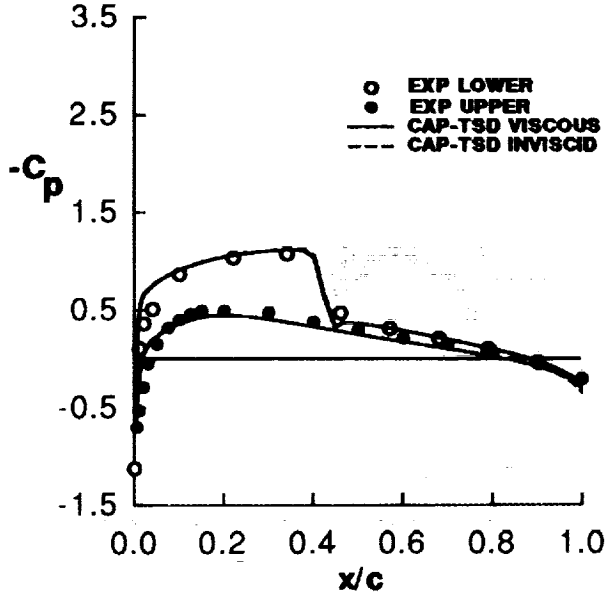

(f) $\alpha = -2.41°$ ↓.

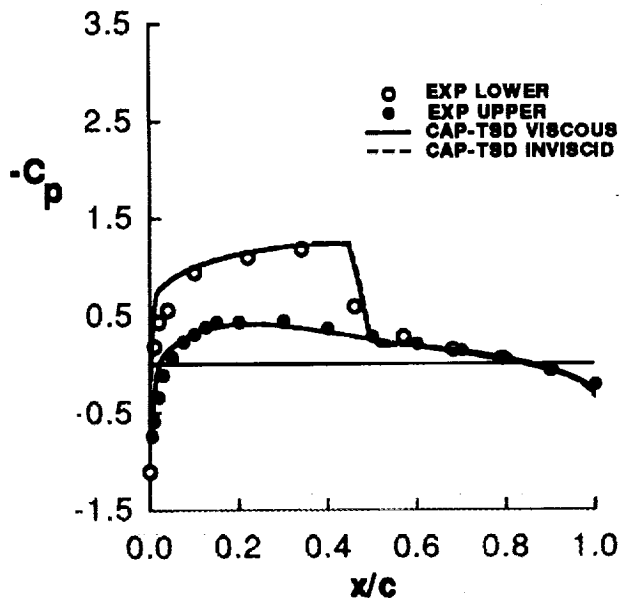

(g) $\alpha = -2.00°$ ↑.

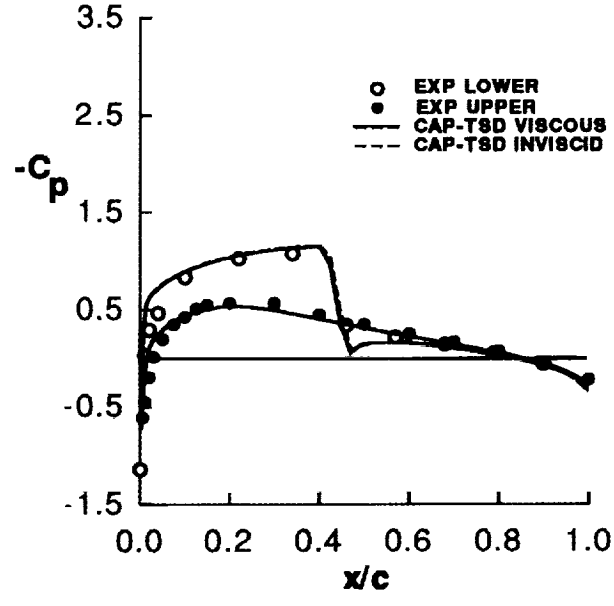

(h) $\alpha = -0.54°$ ↑.

Figure 9. Concluded.

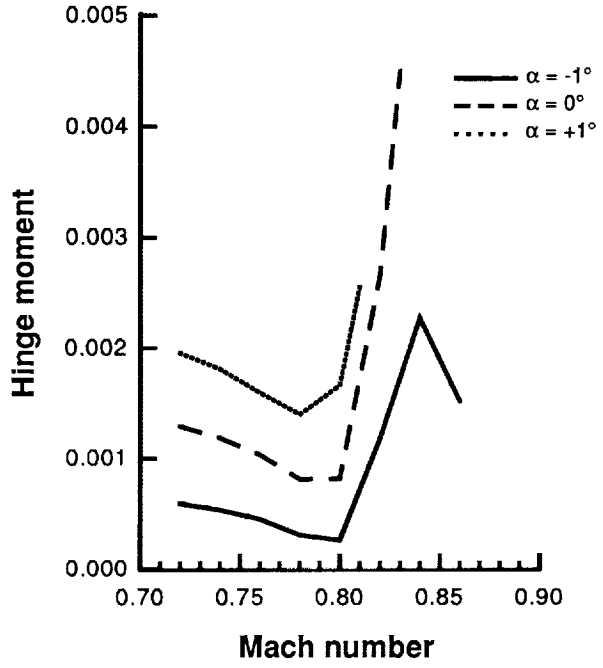

Figure 10. Variation of calculated aileron hinge moment with Mach number for airfoil on the P-80 at three angles of attack with undeflected flap.

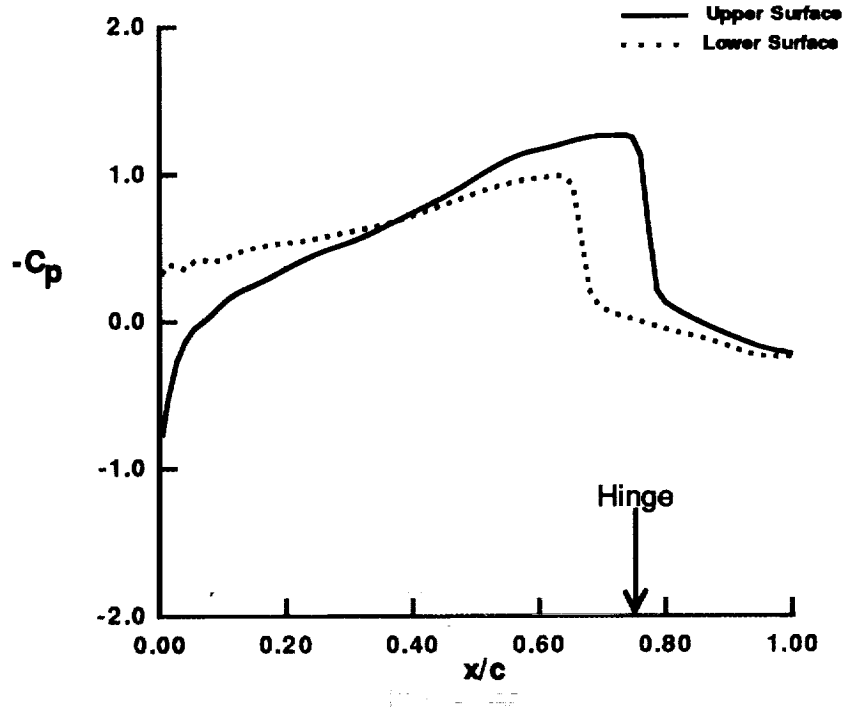

Figure 11. Steady pressure distribution for airfoil on the P-80. $M = 0.82$; $\alpha_0 = 0°$.

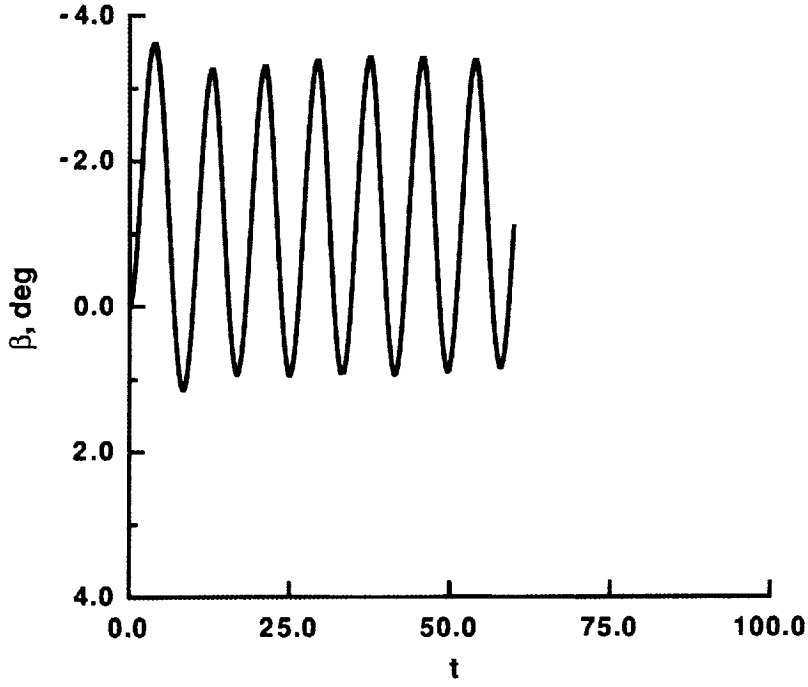

Figure 12. Typical calculated aileron buzz oscillation for airfoil on the P-80 released from undeflected position. $M = 0.8243$; $\alpha_0 = 0°$; $\Delta t = 0.01$.

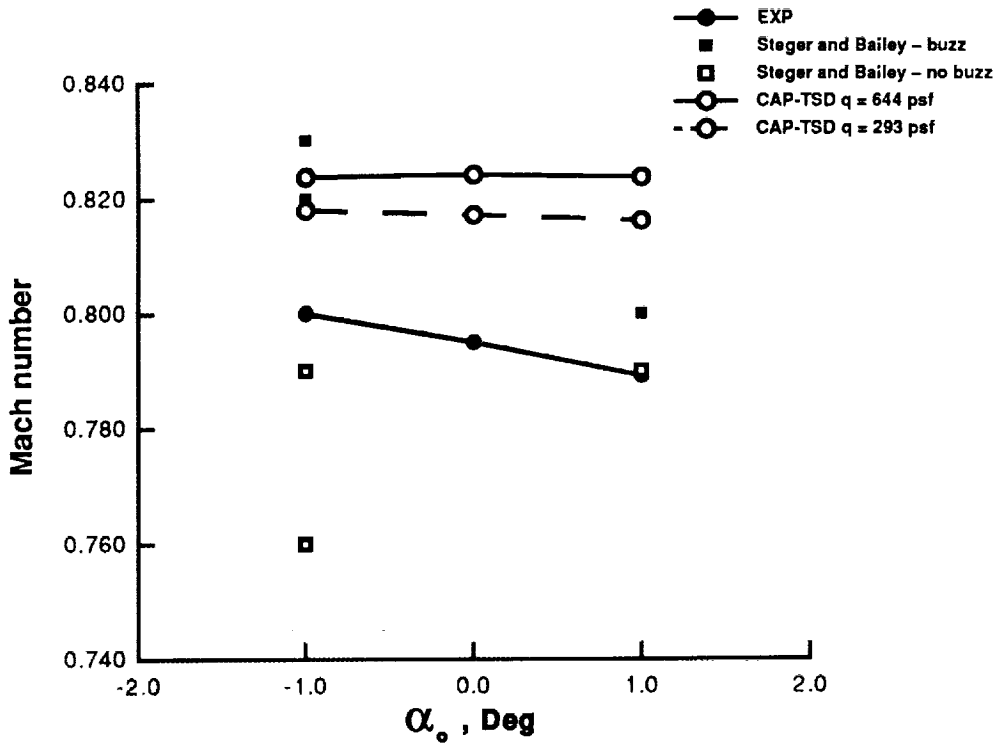

Figure 13. Calculated buzz boundaries for airfoil on the P-80 released from undeflected position compared with experimental results and Navier-Stokes calculations.

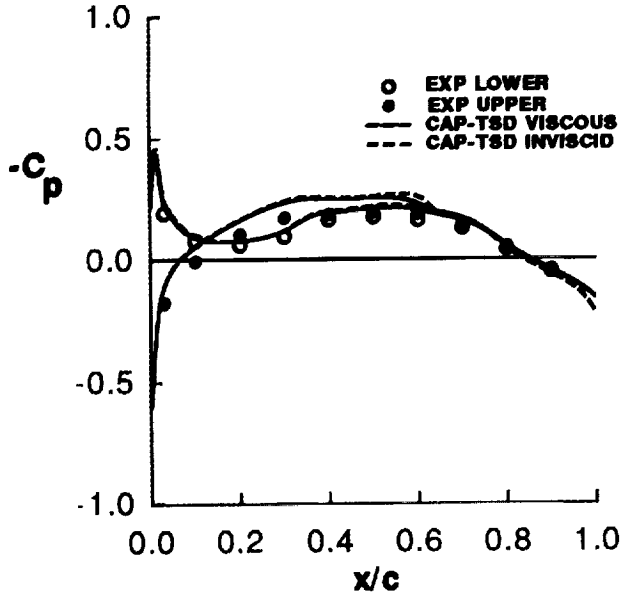

(a) $\eta = 0.181$.

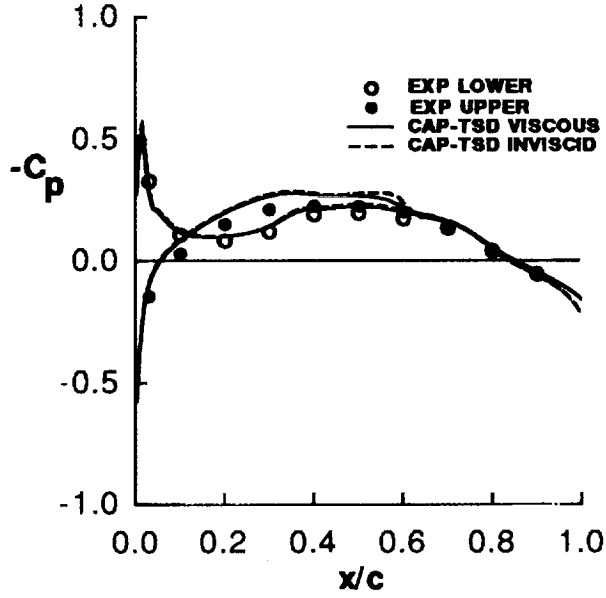

(b) $\eta = 0.355$.

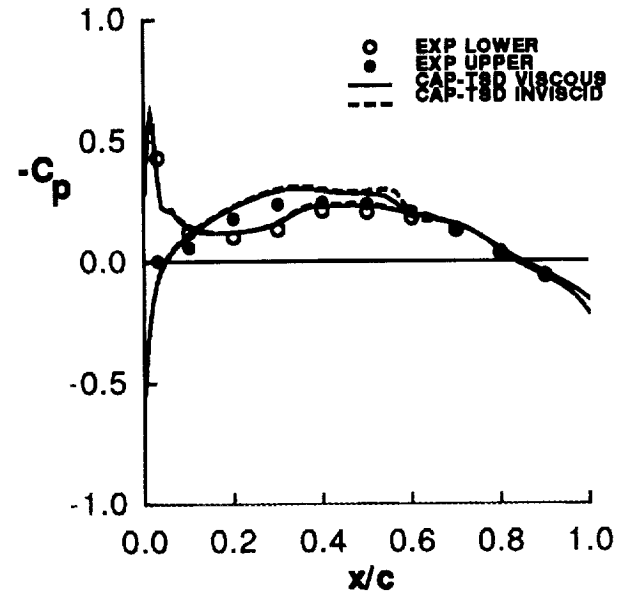

(c) $\eta = 0.512$.

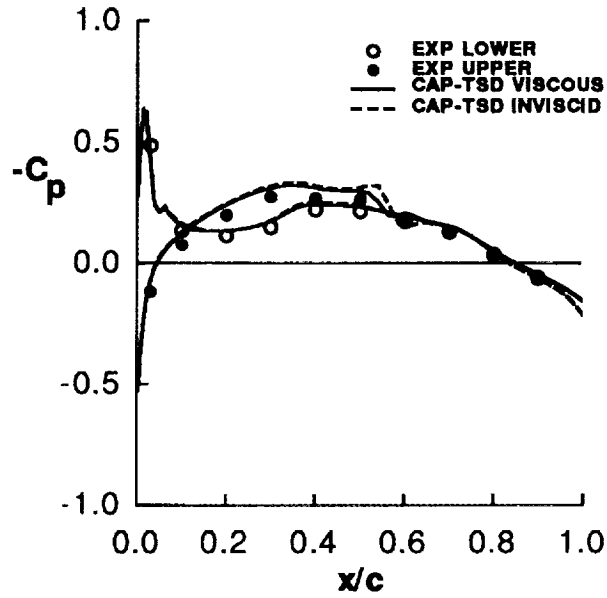

(d) $\eta = 0.641$.

Figure 14. Comparison of calculated and experimental steady pressure distributions for F-5 wing. $M = 0.897$; $\alpha_0 = -0.004°$.

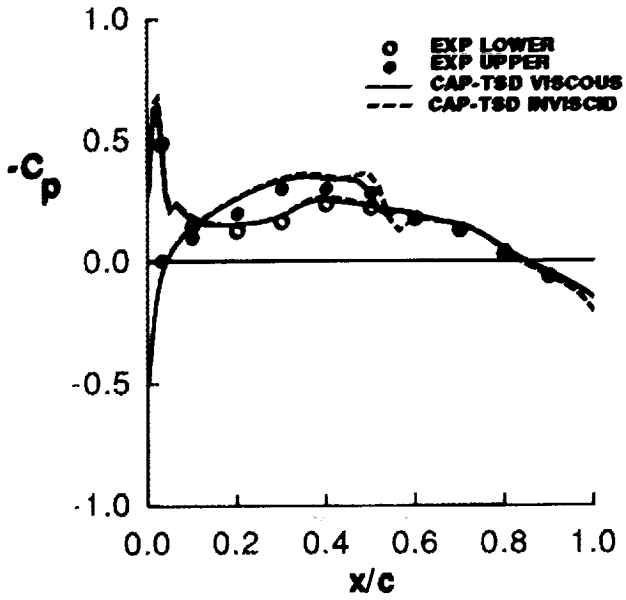

(e) $\eta = 0.721$.

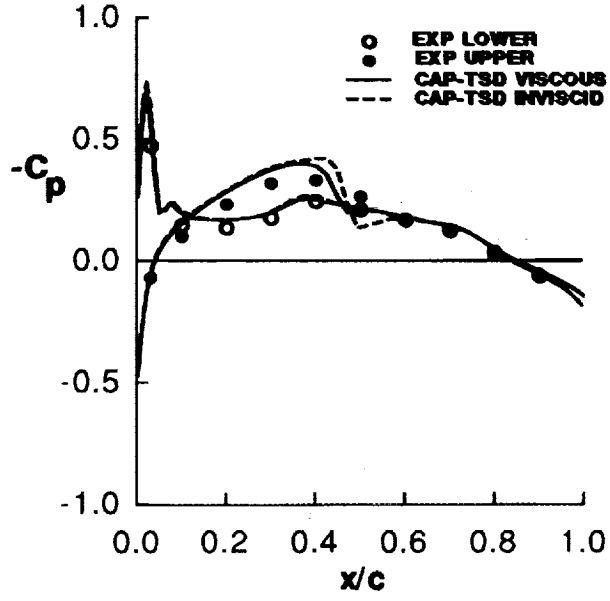

(f) $\eta = 0.817$.

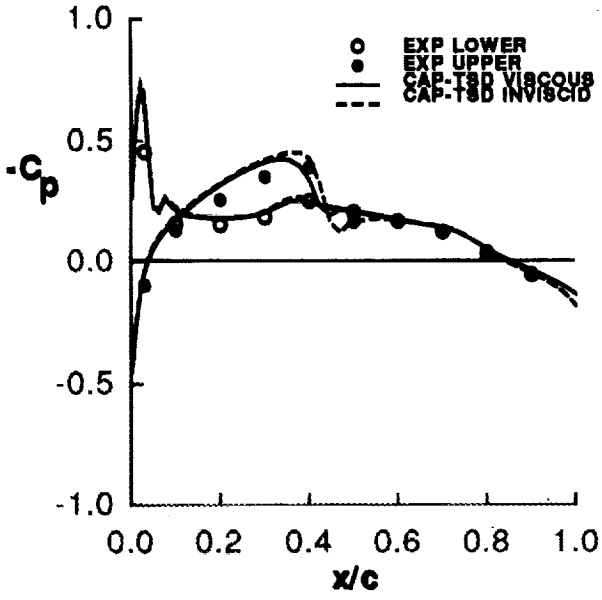

(g) $\eta = 0.875$.

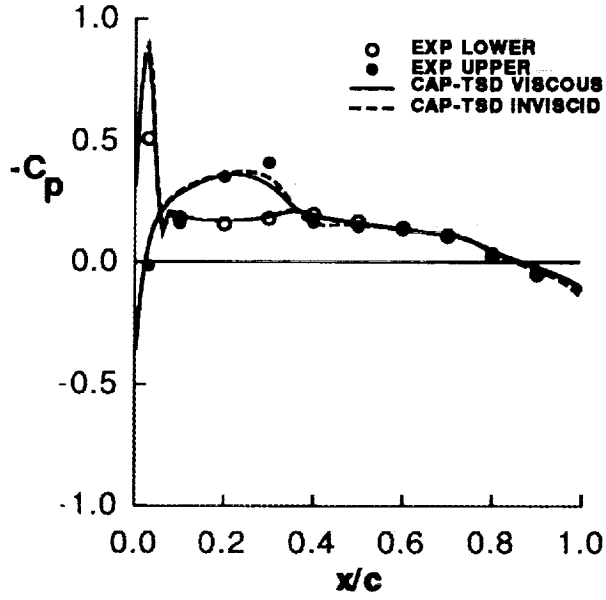

(h) $\eta = 0.977$.

Figure 14. Concluded.

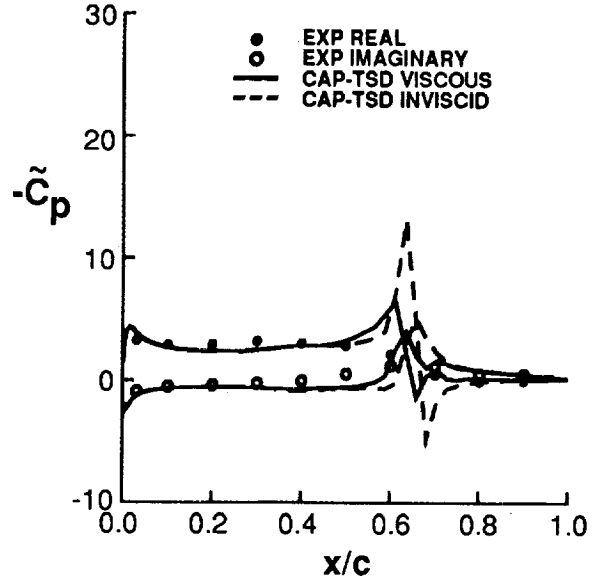

(a) $\eta = 0.181$.

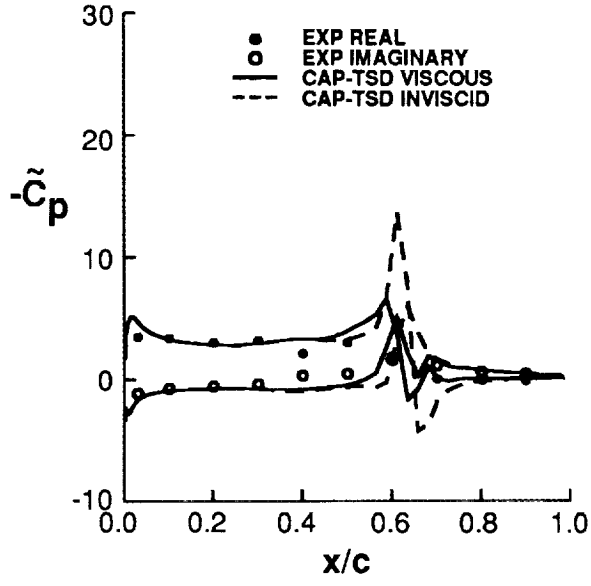

(b) $\eta = 0.355$.

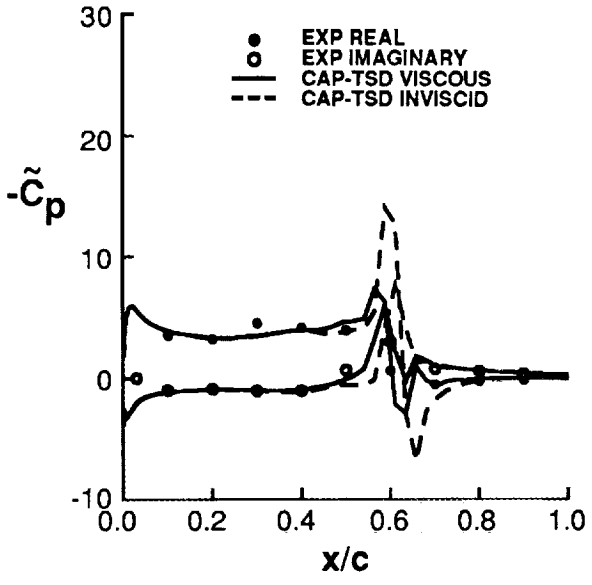

(c) $\eta = 0.512$.

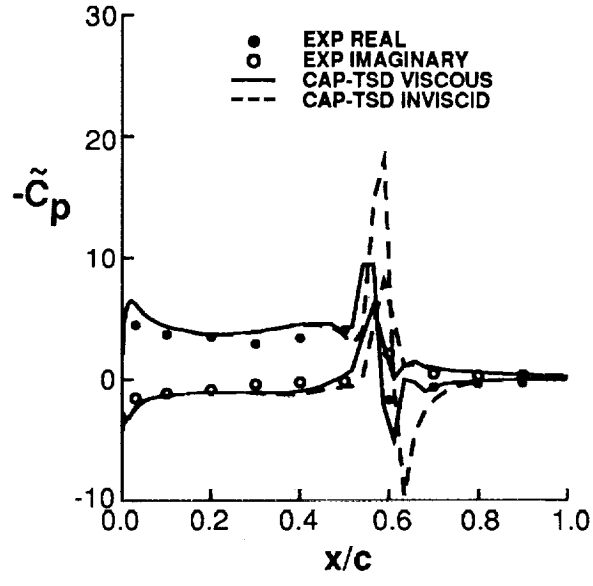

(d) $\eta = 0.641$.

Figure 15. Comparison of calculated and experimental unsteady pressure distributions for upper surface of F-5 wing. $M = 0.899$; $k = 0.137$; $\alpha_0 = 0.002°$; $\alpha_1 = 0.109°$.

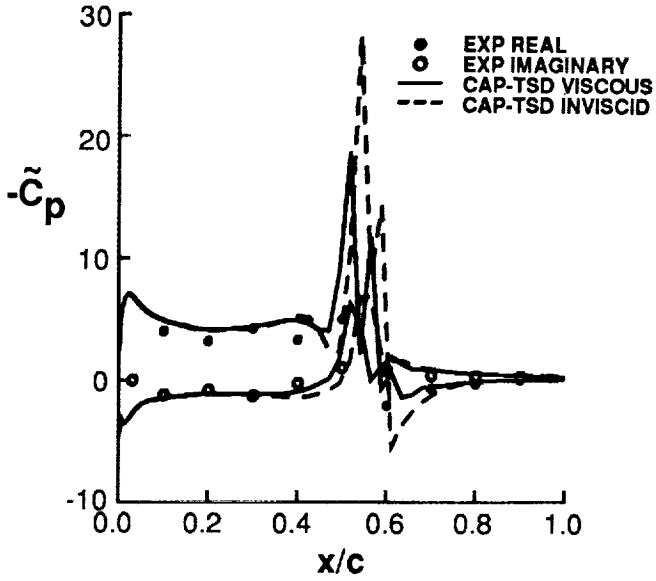

(e) $\eta = 0.721$.

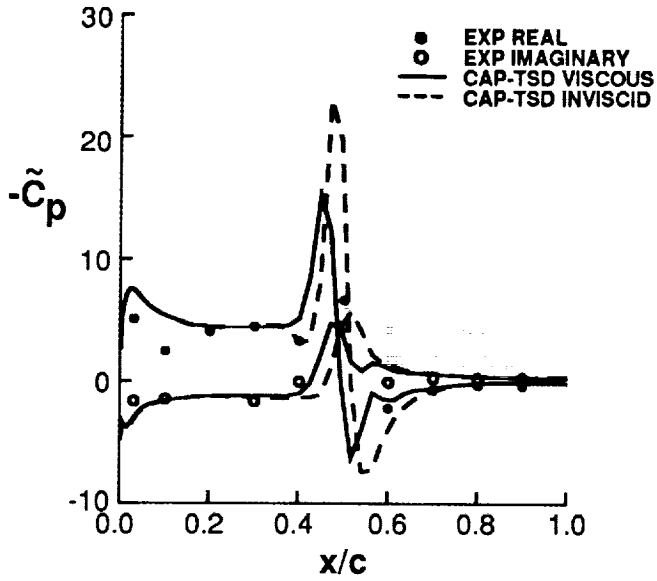

(f) $\eta = 0.817$.

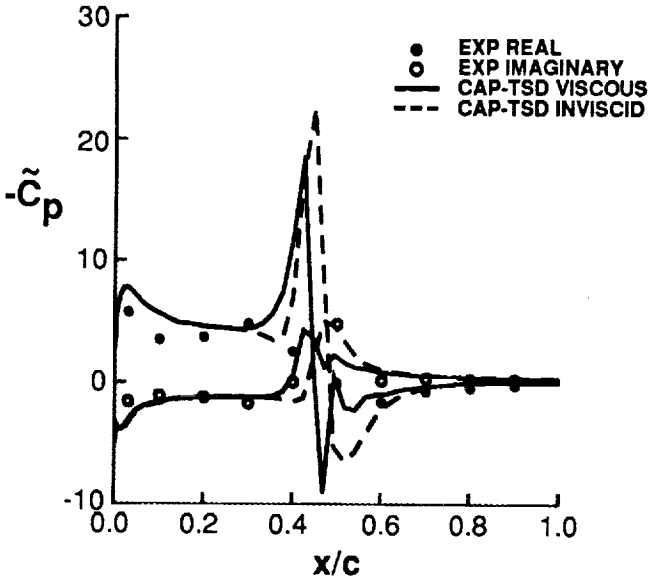

(g) $\eta = 0.875$.

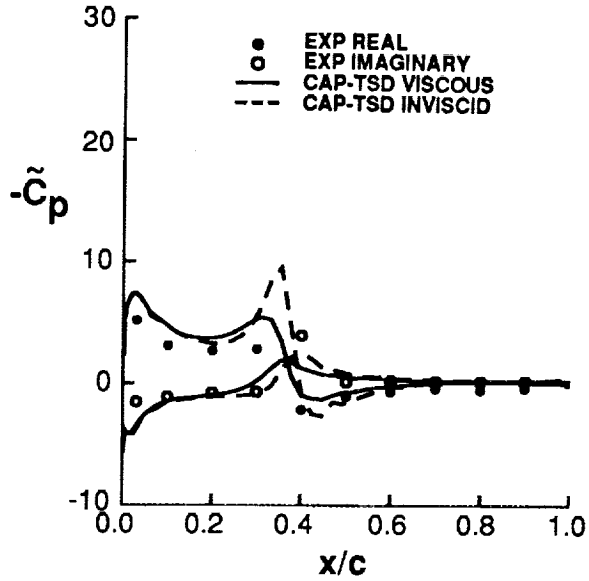

(h) $\eta = 0.977$.

Figure 15. Concluded.

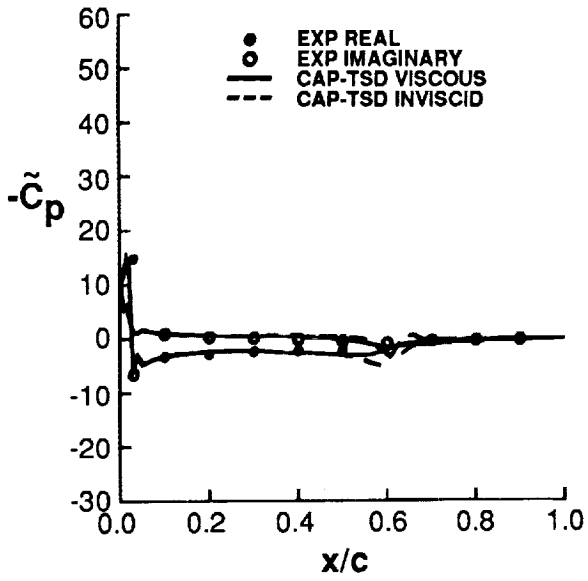

(a) $\eta = 0.181$.

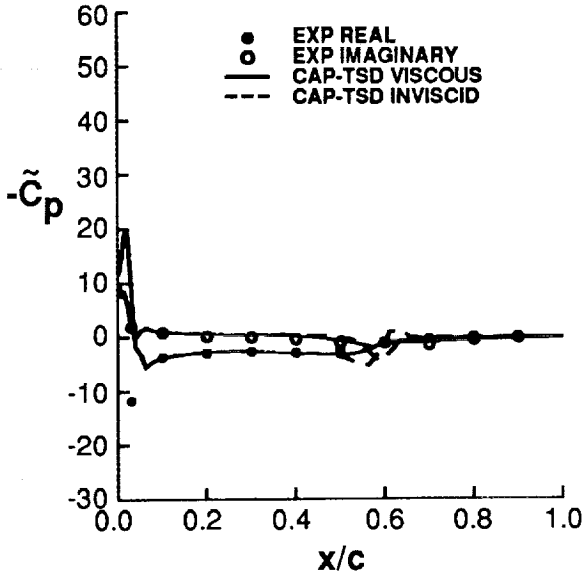

(b) $\eta = 0.355$.

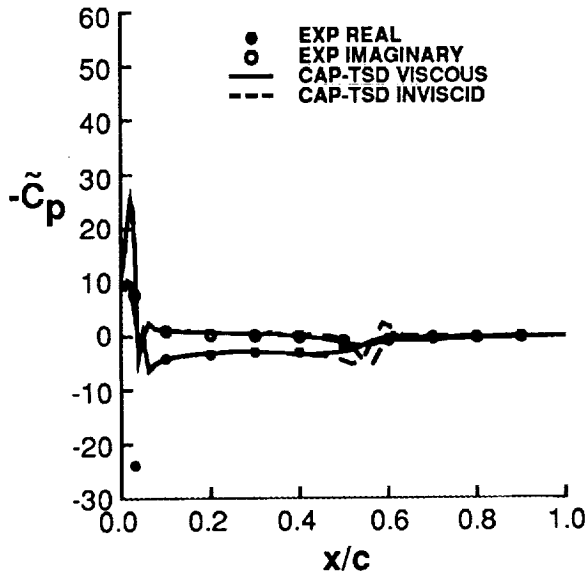

(c) $\eta = 0.512$.

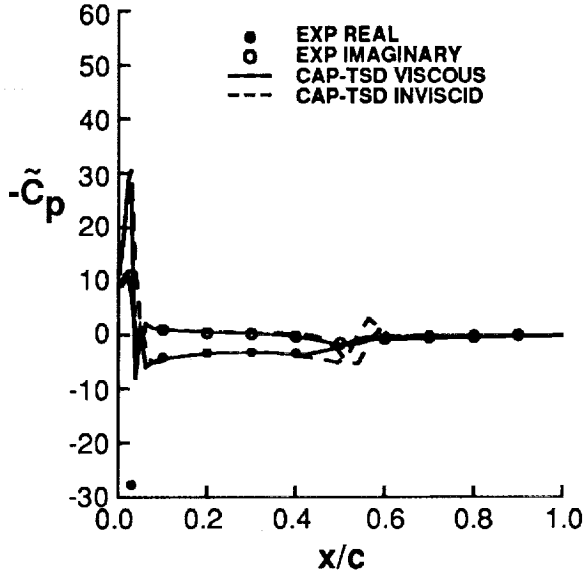

(d) $\eta = 0.641$.

Figure 16. Comparison of calculated and experimental unsteady pressure distributions for lower surface of F-5 wing. $M = 0.899$; $k = 0.137$; $\alpha_0 = 0.002°$; $\alpha_1 = 0.109°$.

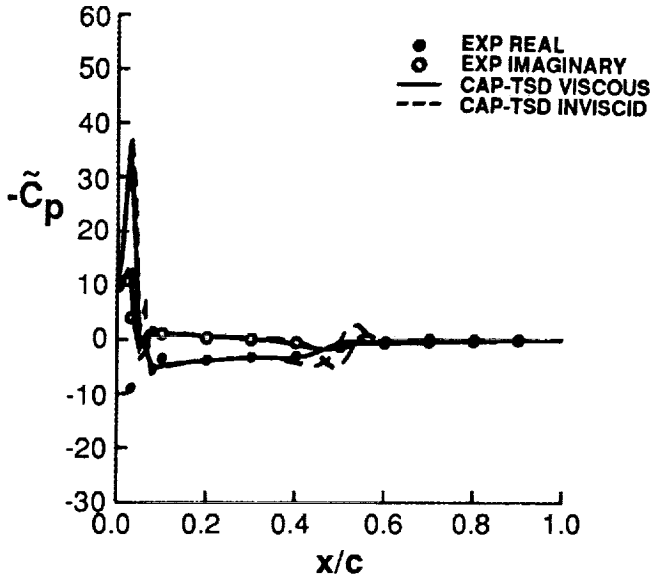

(e) $\eta = 0.721$.

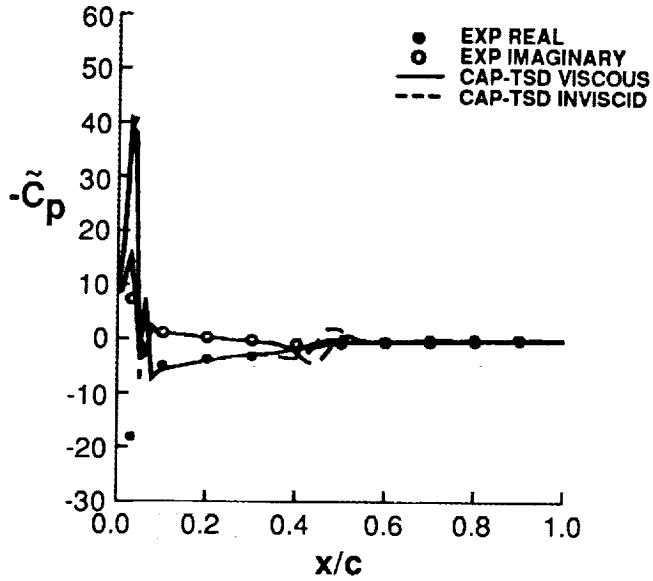

(f) $\eta = 0.817$.

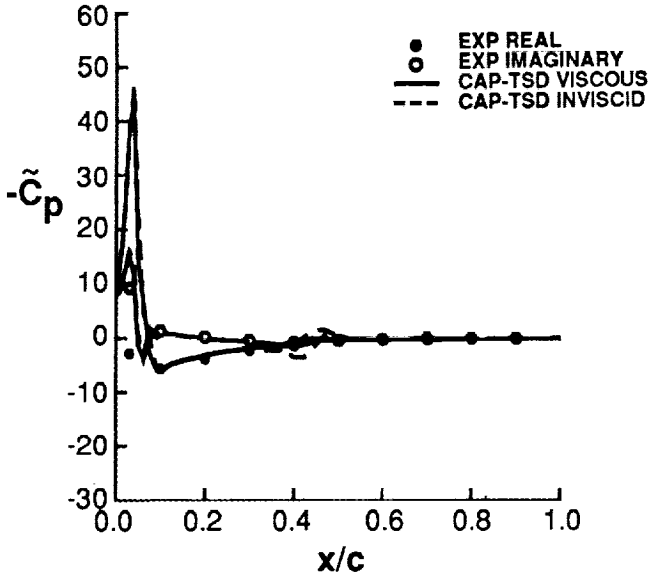

(g) $\eta = 0.875$.

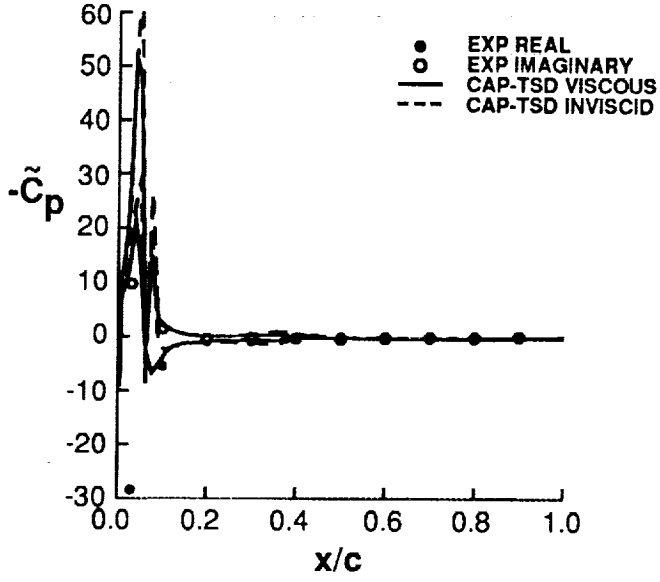

(h) $\eta = 0.977$.

Figure 16. Concluded.

REPORT DOCUMENTATION PAGE

Form Approved
OMB No. 0704-0188

1. AGENCY USE ONLY *(Leave blank)*	2. REPORT DATE	3. REPORT TYPE AND DATES COVERED
	June 1992	Technical Paper

4. TITLE AND SUBTITLE
Calculation of Unsteady Transonic Flows With Mild Separation by Viscous-Inviscid Interaction

5. FUNDING NUMBERS
WU 509-10-02-03

6. AUTHOR(S)
James T. Howlett

7. PERFORMING ORGANIZATION NAME(S) AND ADDRESS(ES)
NASA Langley Research Center
Hampton, VA 23665-5225

8. PERFORMING ORGANIZATION REPORT NUMBER
L-16996

9. SPONSORING/MONITORING AGENCY NAME(S) AND ADDRESS(ES)
National Aeronautics and Space Administration
Washington, DC 20546-0001

10. SPONSORING/MONITORING AGENCY REPORT NUMBER
NASA TP-3197

11. SUPPLEMENTARY NOTES

12a. DISTRIBUTION/AVAILABILITY STATEMENT
Unclassified Unlimited

Subject Category 02

12b. DISTRIBUTION CODE

13. ABSTRACT *(Maximum 200 words)*

This paper presents a method for calculating viscous effects in two- and three-dimensional unsteady transonic flow fields. An integral boundary-layer method for turbulent viscous flow is coupled with the transonic small-disturbance potential equation in a quasi-steady manner. The viscous effects are modeled with Green's lag-entrainment equations for attached flow and an inverse boundary-layer method for flows that involve mild separation. The boundary-layer method is used stripwise to approximate three-dimensional effects. Applications are given for two-dimensional airfoils, aileron buzz, and a wing planform. Comparisons with inviscid calculations, other viscous calculation methods, and experimental data are presented. The results demonstrate that the present technique can economically and accurately calculate unsteady transonic flow fields that have viscous-inviscid interactions with mild flow separation.

14. SUBJECT TERMS	15. NUMBER OF PAGES
Viscous-inviscid interaction; Transonic unsteady aerodynamics; Aileron buzz; Boundary layer	37
	16. PRICE CODE A03

17. SECURITY CLASSIFICATION OF REPORT	18. SECURITY CLASSIFICATION OF THIS PAGE	19. SECURITY CLASSIFICATION OF ABSTRACT	20. LIMITATION OF ABSTRACT
Unclassified	Unclassified		

NSN 7540-01-280-5500

Standard Form 298(Rev. 2-89)
Prescribed by ANSI Std. Z39-18
298-102

NASA-Langley, 1992